IEEE Access
Multidisciplinary ⋮ Rapid Review ⋮ Open Access Journal

Received 3 December 2022, accepted 30 January 2023, date of publication 1 February 2023, date of current version 7 February 2023.

Digital Object Identifier 10.1109/ACCESS.2023.3241458

TOPICAL REVIEW

High-Performance Multiband Ambient RF Energy Harvesting Front-End System for Sustainable IoT Applications–A Review

YI CHEN LEE[1], HARIKRISHNAN RAMIAH[1], (Senior Member, IEEE), ALEXANDER CHOO[1], (Graduate Student Member, IEEE), KISHORE KUMAR PAKKIRISAMI CHURCHILL[1], (Graduate Student Member, IEEE), NAI SHYAN LAI[2], CHEE CHEOW LIM[2], YONG CHEN[3], (Senior Member, IEEE), PUI-IN MAK[3], (Fellow, IEEE), AND RUI P. MARTINS[3,4], (Fellow, IEEE)

[1]Department of Electrical Engineering, Faculty of Engineering, University of Malaya, Kuala Lumpur 50603, Malaysia
[2]School of Engineering, Asia Pacific University of Technology and Innovation, Kuala Lumpur 57000, Malaysia
[3]State-Key Laboratory of Analog and Mixed-Signal VLSI, Faculty of Science and Technology-ECE, Institute of Microelectronics, University of Macau, Macau, China
[4]Instituto Superior Técnico, Universidade de Lisboa, 1649-004 Lisbon, Portugal

Corresponding author: Harikrishnan Ramiah (hrkhari@um.edu.my)

This work was supported in part by the Research University (RU) Grant through the Faculty Program under Grant GPF056B-2020, in part by the Partnership Grant MG012-2022; and in part by the Science and Technology Development Fund, Macau, SAR, under Grant FDCT 0036/2020/AGJ and Grant SKL-AMSV(UM)-2020-2022.

ABSTRACT The increasing demand for wireless Internet of Things (IoT) calls for power efficient RF energy harvesting approach. The current dominant single-band RF energy harvesting front-end system restricts itself to a single frequency, which is at the risk of ineffective operation when the harvesting frequency is unavailable. This paper reviews and explores the alternative approach of a multiband RF energy-harvesting front-end system. It covers all essential circuitry of a multiband RF energy harvesting front-end system, starting from the recent RF surveys which investigate the typical, usable, and high-strength RF input, to the overview of the state-of-the-art antenna, impedance matching network (IMN), and RF-DC rectifier. The recent advancement of the multiple RF input harvesting abilities, reflection loss minimization, and performance improvement are comprehensively reviewed for different operating conditions, and this review also presents the advantages and disadvantages of the different circuit architecture combinations for multiband RF energy harvesting front-end systems. In summary, this review aims to fill the research gap in the further advancement of multiband RF energy harvesting towards enhancing its performance through optimal circuit integration of the front-end system.

INDEX TERMS CMOS, power conversion efficiency (PCE), multiband RF energy harvesting, RF power transmission.

I. INTRODUCTION

The rising of the Industrial Revolution 4.0 (IR 4.0) [1] imposes a massive amount of compact wireless sensors to provide seamless data exchange between humans and machines. The energy demand thus becomes insatiable. Conventional battery-operated devices require costly battery replacement which further exacerbates safety [2] and environmental concerns [3]. Harvesting ambient energies to self-power the devices prove to be crucial for long-term sustainability [4]. The common types of energy harvesting solutions are solar [5], vibration [6], sound [7], and radio frequency (RF) [8], [9].RF is the most beneficial energy source today as the wireless communication system has been advancing rapidly due to the initialization of 5th Generation (5G) wireless communication. Many electronic

The associate editor coordinating the review of this manuscript and approving it for publication was Jie Tang.

devices follow the massive growth trend of Information and Communication Technology (ICT) and the Internet of Things (IoT) [10], [11], [12]. Electronic devices enabled with internet have contributed to the overall increase of density in RF frequency propagated in free space. This proliferates the opportunity for wireless power transfer and energy harvesting. Hence, the recent trend in research interest is to implement self and wirelessly powered low-power electronic devices, such as wireless sensor nodes (WSN), by harvesting RF energy [2]. The on-chip integration of RF energy harvesting (RFEH) system would have considerable potential to realize a miniaturized and battery-less electronic solution for healthcare wearables, biometric sensors, automotive sensors, and other industrial applications [13], [14], [15].

The RFEH system can be categorized into front-end [16], [17], [18], [19] and back-end [20], [21], [22], [23] solutions. A front-end RFEH system consists of an RF receiver antenna, an impedance matching network, and an RF-DC rectifier as shown in Fig. 1. The front-end solution is responsible to harvest and convert the RF power into DC power. For instance, for a front-end system with 40% power conversion efficiency at −10 dBm, the output DC power is only 40 μW. In this case, the front-end system is at risk in harvesting insufficient power to start-up sensor devices, in which the start-up power expands from 10 μW up to 100 μW [24]. To compensate for this bottleneck, the back-end RFEH system is integrated to boost or pump up the DC current from the front-end RFEH system and provide sufficient output current to power up the sensor devices. Since the front-end and back-end RFEH system has different functionality and adopts different design approaches, the front-end and back-end are often separated in the discussion. Therefore, the scope of this review is targeted at the front-end of the RFEH system.

Much research work on single-band RFEH systems has reported encouraging performance in the context of high power conversion efficiency (PCE), wide power dynamic range (PDR), and high sensitivity [8], [9]. However, several limitations for the single-band RFEH systems are yet to be addressed, such as capped single-band signal power and overreliance on the single-band source. In [25], any single-band signal power is limited by the surrounding usage, leading to a maximum scale in harvesting power. At the same time, ambient single-band RF energy suffers from fluctuating power density, potentially lowering the harvested signal power. Low harvested ambient signal power significantly restricts the rectifier's power transfer performance. Thus, harvesting from multiple RF bands which are known as the multiband RFEH systems has been proposed to fulfill the power demands [26] and to maximize the output power [27], [28].

This article focuses on the investigation of the RFEH front-end system, especially the multiband RFEH front-end system. Section II discusses the recent RF surveys in the ambient environment. Section III briefly overviews the RFEH front-end circuit architecture. Section IV reviews the recently reported designs for multiband RFEH front-end circuitry. Section V discusses the circuit integration of the multiband RFEH front-end system. Section VI concludes this review paper.

II. AMBIENT RF POWER

The presence of ambient RF power is mainly due to wireless power transmission which propagates electromagnetic power over a distance from the transmitter to the receiver at free space. In wireless transmission, the transmitter converts the electrical power into RF power which is transmitted to the receiver. The scavenging of the RF power residue in the free space medium is known as RF energy harvesting [29]. RF energy harvesting can be further classified into near-field and far-field which differ based on the propagation distance. The propagation distance less than Fraunhofer Distance is considered as near-field whereas the propagation distance more than Fraunhofer Distance is known as far-field [30]. The Fraunhofer Distance can be expressed as [30]:

$$Fraunhofer\ Distance = \frac{2D^2}{\lambda} \tag{1}$$

where $\boldsymbol{D}$ is the diameter of the antenna and $\boldsymbol{\lambda}$ is the wavelength of the RF wave.

In general, both near-field and far-field energy harvesting requires a transmitter (Tx), a medium, and a receiver (Rx). Near-field energy harvesting is the transfer of power at a short distance, generally through a magnetic field such as magnetic coupling or resonance of inductors or coils [9]. A transformer is the simplest way to explain the concept of near-field energy harvesting. Assume a basic near-field application in which the transmitter consists of the primary coil while the receiver consists of the secondary coil. The AC power is transferred from the primary coil to the secondary coil through magnetic induction where the medium is the magnetic field. Battery charging through near-field wireless power transfer via magnetic resonance is reported in [31].

Alternately, far-field propagation is the transfer of power at a long distance, generally through the transmission and reception of antennas. In theory, long-distance transmission leads to lower input power density. This is due to the RF wave which has an inverse square law spreading characteristic, which indicates that the power transfer is inversely proportional to the square of the distance. The loss during the free space transmission is known as the free space path loss (FSPL). In effect to the FSPL, far-field energy harvesting has lower input power density than near-field energy harvesting. The input power density can be computed with the aid of the Friis transmission equation.

$$P_R = \frac{P_T G_T G_R c^2}{(4\pi D f)^2} \tag{2}$$

where P_R and P_{T} represents the input received and transmitted power, G_R and G_T represents the gain of the receiver antenna and transmitter antenna, c is the speed of light, D is the frequency wave transmission distance between the

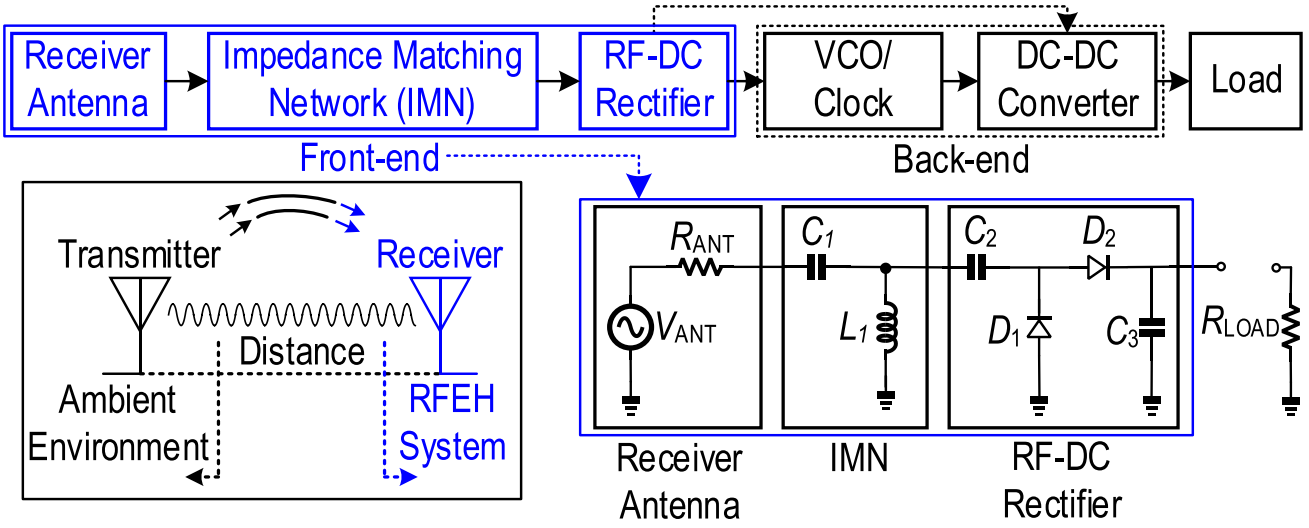

FIGURE 1. General front-end RFEH system.

transmitter and receiver and f is the frequency of the RF wave. From (2), it is apparent that harvesting RF power at lower frequency results in higher input received power. However, this statement is not entirely accurate. The signal crowding strength of different RF bands should also be a factor of consideration. This is due to the inconsistency and volatile characteristic of the RF signal's strength. In brief, the usage and environmental factors affect signal strength [22].

The radio spectrum expands from 3 kHz to 300 GHz [32] which can be further classified into several RF bands. The density of use in the RF bands relies on the RF consumption level. A highly utilized RF band increases the scale of RF power residue in the ambient environment, leading to higher RF power density. In general, the highly utilized ambient RF bands are the Very High-Frequency band (VHF), Ultra High-Frequency band (UHF), and Super High-Frequency band (SHF) ranging from 30 MHz to 30000 MHz, which capture most of the RF applications such as GSM 2G, UMTS 3G, LTE 4G, 5G NR, ISM, WIFI-Communication, FM broadcasting, and Bluetooth.

Two main constraints are limiting the signal strength and power density of RF signals. First, the non-uniform establishment of RF facilities can affect the overall power density of the RF signals in urban, suburban, or rural areas [33], [34]. Second, the presence of blocking obstacles such as tall buildings or mountains can degrade the strength of the RF signals [35].

The RF survey summarizes the signal strength for different frequency bands detected in the ambient, measured at metro stations and residential areas in London [36], indoor and outdoor of University Covilha [37], and semi-urban and urban locations in London [38]. Fig. 2 shows the power density measured at the Northfields London Underground station [38]. The frequency bands presented in Fig. 2 are highly recommended references in designing an RF energy harvesting system due to higher RF power density.

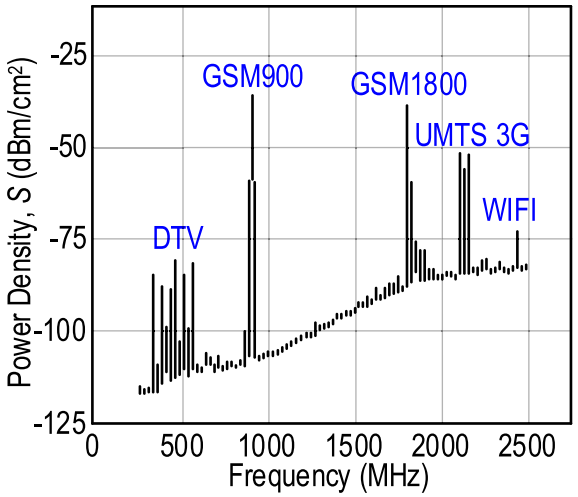

FIGURE 2. Input RF power density measured outside the Northfields London Underground Station [38] (redraw noiseless simplified version).

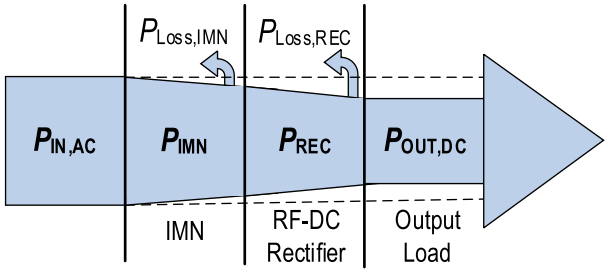

FIGURE 3. Power transfer process.

III. RFEH FRONT-ENDS ARCHITECTURE

In general RFEH front-end circuits, consist of three main components which are the RF receiver antenna, the impedance matching network, and the RF-DC rectifier. The RF receiving antenna functions to receive the AC signal at the dedicated frequency band. The received signal is

subsequently passed to the impedance-matching network for maximum power transfer achieved by minimizing the reflection loss. The matching network also acts as a passive voltage-boosting block, realized by the inductor at the IMN. Thereafter, the AC signal is transferred to the RF-DC rectifier to convert the RF power into a DC output (ideally ripple-free). The entire power transfer process of the RF energy harvesting front-end circuit is conceptually shown in Fig. 3. Some predictable losses incurs during the end-to-end transfer of the received power. Considering the losses, the output DC power can be written as:

$$P_{OUT,DC} = P_{IN,AC} - P_{LOSS,IMN} - P_{LOSS,REC} \quad (3)$$

where $\boldsymbol{P_{OUT,DC}}$ is the output DC power and $\boldsymbol{P_{IN,AC}}$ is the input received AC power. $\boldsymbol{P_{LOSS,IMN}}$ is the losses from the impedance matching network and $\boldsymbol{P_{LOSS,REC}}$ is the losses from the rectifier. Parasitic resistance of the components in use such as the capacitor, inductor or transistor contributes to the losses during the power transfer process.

A. RF RECEIVER ANTENNA

The review scope in this section is limited to the RF receiver antenna, which functions in receiving and converting the ambient RF energy into an electrical signal. An optimally designed antenna can boost the system's performance by providing higher input power. The peak input voltage, $\boldsymbol{V_{ANT}}$ of the receiver antenna can be calculated from [39]:

$$V_{ANT} = \sqrt{8 \times R_{ANT} \times P_R} \quad (4)$$

where $\boldsymbol{R_{ANT}}$ is the series resistance of the receiver antenna and $\boldsymbol{P_R}$ is the available input received power at the receiver antenna.

For the RFEH application, the RF receiver antenna consists of three main parameters which are the operating frequency, gain, and size. The operating frequency of the RF receiver antenna specifies the frequency band to be harvested by the receiver antenna. Harvesting a non-operating frequency band will lower the input received power for the system. The gain of the RF receiving antenna specifies the performance of the antenna in scavenging the power from the operating frequency. A high-gain antenna increases the received power which enhances the overall RFEH system [40]. The gain of the antenna can be calculated from [41]:

$$Gain, G = \varepsilon_R D \quad (5)$$

where $\boldsymbol{G}$ is the antenna gain, $\boldsymbol{\varepsilon_R}$ is the radiation efficiency and $\boldsymbol{D}$ is the antenna directivity. The antenna directivity relates to the radiation pattern and polarization of the antenna. The antenna's radiation pattern and polarization define the antenna's capability to capture the ambient RF wave power. An antenna can radiate in a unidirectional pattern or omnidirectional pattern. For harvesting ambient RF energy whose incident angle is unknown, the omnidirectional pattern with a broad effective angle signal coverage can outperform the unidirectional pattern. However, the trade-off for implementing the omnidirectional pattern is the lower antenna gain [42], [43]. Besides the radiation pattern, the polarization of the antenna can affect the antenna gain. The antenna's polarization consists of linear polarization (LP), circular polarization (CP) and elliptical polarization (EP). To obtain high gain, the mismatch in the polarization of the transmitter and receiver antenna must be avoided [44]. The size of the RF receiver antenna indicates the space required to install the antenna, and usually relates to the antenna efficiency. Referring to [45], a smaller physical size of the antenna can reduce the antenna gain. However, the design trend of antenna concentrates on achieving a lower profile, which is also known as the miniaturization of the antenna. Therefore, it is a trade-off to be considered when designing or selecting the RF receiver antenna. The relationship between the compactness, gain and size is given as [46]:

$$Compactness \propto \frac{G}{A} \quad (6)$$

where $\boldsymbol{G}$ is the antenna measured gain and $\boldsymbol{A}$ is the antenna size.

From [47], there are several distinct antenna types and shapes for RF receiver antenna. The most preferred type is the printed antennas especially printed planar patch antennas [48] due to their compact size, high versatility, and high flexibility in integrating with rectifier circuits [47]. Basic shapes such as rectangular, square, or circular are the fundamental shape for the planar patch antenna. However, the basic shape planar patch antenna suffers from limited gain and bandwidth. To enhance the performance of the planar patch antenna, modifications to the basic shape have been proposed. The popular modification is through the implementation of slotted design [49], [50], [51], employing fractal geometry [52], [53], or designing a unique-shaped antenna [24], [54], [55], [56], [57], [58], [59].

The slotted antenna design introduces holes or gap intervals inside the basic shapes, increasing the current path and leading to the increase of gain [60]. By adopting a slotted design, the work [49], [50], [51] measures a peak gain of 8.25 dBi, 4.3 dBi and 5 dBi respectively when cutting through a cross-shaped slot, c-shaped slot and e-shaped slot from the conventional basic shape patch antenna.

The fractal antenna implements a fractal geometry pattern in the patch antenna. The popularly used fractal geometry for RF receiver antenna is the Koch snowflake geometry [52], [53]. The design in [52] and [53] proposed a 4-iteration order and 6-iteration order Koch fractal structure with a peak measured gain of 4.5 dBi and 3.1 dBi respectively. Practically, an increment in the iterations order can increase the overall effective length which leads to a higher realized gain [53]. However, the increment in the iteration order also increases the complexity of the pattern, contributing to a trade-off of difficulty in fabrication [61].

The unique-shaped antenna introduces unique-shaped patterns such as T-shaped [54], Folded-shaped [55], Yagi-Uda [56],and Loop [24], [57], [58], [59] in the design of the antenna. In [54], an 866 MHz single-band antenna has

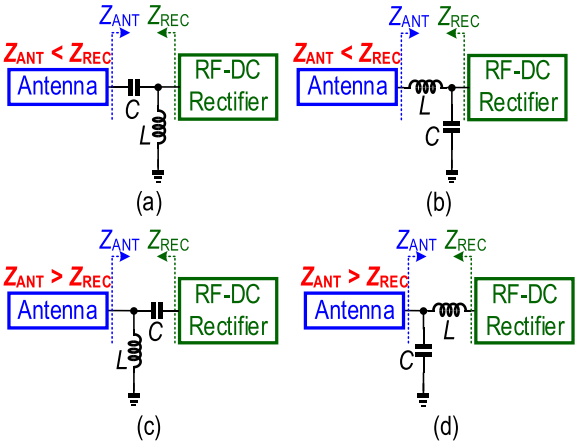

FIGURE 4. Types of L-matching network: (a) High-pass upward load impedance transformation. (b) Low-pass upward load impedance transformation. (c) High-pass downward load impedance transformation. (d) Low-pass downward load impedance transformation.

been realized by implementing a T-shaped monopole with a coplanar waveguide feeding line, which exhibits dipole-like radiation and measures a peak gain of 2 dBi. The work [55] fully utilized the folded technique by folding the two poles, contributing to a reduction in the antenna diameter. At the same time, this folded dipole design achieved a measured gain of 1.84 dBi. Alternately, the Yagi-Uda design [56] enables a high measured gain of 7 dBi at 950 MHz. However, the Yagi-Uda structure consists of several parallel branches which require more size, hence reducing the overall antenna compactness. The loop antenna is one of the most popular antenna designs for the application of RF energy harvesting [58], [59]. In [24], a compact square loop antenna has been introduced to harvest from 868 MHz. This square loop antenna design is horizontally polarized and capable of achieving a peak gain of 0.66 dBi with a tiny antenna diameter of 34 mm. Furthermore, [57] proposed a novel meander line structure loop antenna that reduces 50% of the size respective to the conventional loop antenna. The reported design can achieve a radiation efficiency of 97% at 925 MHz, leading to a peak antenna gain of 4.22 dBi.

B. IMPEDANCE MATCHING NETWORK

In the RFEH system, frequent high impedance variation occurs due to the use of non-linear devices such as diodes or transistors in the rectifier. Therefore, an impedance-matching network is integrated after the antenna to minimize the reflection loss due to impedance mismatch. In general, an impedance matching network follows a common working principle, where the real component of two integrating blocks is equal while the imaginary component of two integrating blocks is in the complex conjugate. Referring to Fig. 4, the mathematical equation can be written as, $Re(Z_{ANT}) \mathcal{D} Re(Z_{REC})$ and $Im(Z_{ANT}) \mathcal{D} Im(Z^*_{REC})$.

A high reflection loss limits the input power of the rectifier, leading to a capped output power. The undesirable capped output power degrades the rectifier's output parameters such

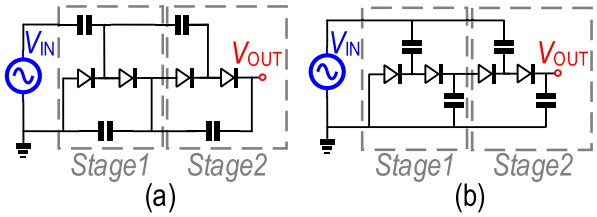

FIGURE 5. Two stages full-wave rectifier: (a) Cockcroft-Walton (Greinacher or Villard). (b) Dickson-type.

as the output voltage, sensitivity and power dynamic range. The numerical value of the signal reflected can be referred to in the reflection coefficient equation given below [62], [22].

$$\Gamma = S_{11,mag} = \frac{Z_{REC} - Z^*_{ANT}}{Z_{REC} + Z^*_{ANT}} \tag{7}$$

where Γ is the value of the reflection coefficient, it is commonly known as the $S_{11,mag}$. Z_{REC} is the impedance of the rectifier which is modeled as $R_{REC} + X_{REC}$, Z_{ANT} is the impedance of antenna which is modeled as $R_{ANT} + X_{ANT}$ and Z^*_{ANT} is the complex conjugate of the antenna impedance. The reflection coefficient is always lesser than 1. Assuming a reflection coefficient of 0.5, it indicates that half of the input power is reflected back. In this case, the system is unmatched. To match two integrating blocks, the reflected power must be less than 10%, which is generally referred as $S_{11,dB}$ less than -10 dB [63].

On-chip impedance matching network adopts the combinations of passive components such as resistors, capacitors, inductors, and transformers. The most frequently used impedance-matching network topologies are the L-matching, Pi-matching, and T-matching [64], with the L-matching network having the highest popularity in use.

An L-matching network consists of a capacitor and inductor in an L-shaped configuration as shown in Fig. 4. In general, the antenna impedance is fixed while the impedance of the rectifier and the load impedance varies respectively to the frequency. Therefore, The L-matching network is responsible to boost up the load impedance when it is lower than the antenna impedance and pulling down the load impedance when it is higher than the antenna impedance. Thus, it contributes to the upward load impedance transformation as shown in Fig. 4(a), 4(b), and downward load impedance transformation as shown in Fig. 4(c), 4(d). Capacitors pass high-frequency signals while the inductors pass the low-frequency signals. Therefore, reversing the location of the capacitor and inductor in an L-matching network realizes a low-pass L-matching and high-pass L-matching transfer function respectively. Fig. 4(a) and Fig. 4(c) show the high-pass L-matching network while Fig. 4(b) and Fig. 4(d) show the low-pass L-matching network.

To implement impedance matching, the simplest approach is to compute the optimized parameters for the components in the matching network [65], [66], [67], [68]. Reference [65] proposed a new analytic model for the Dickson charge pump rectifier which includes the optimum design parameters for

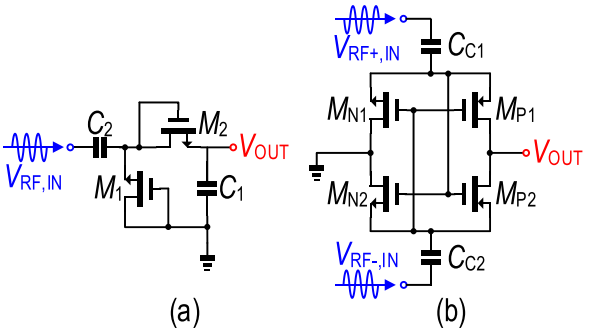

FIGURE 6. General rectifier topology: (a) Dickson-type. (b) CCDD-type.

the matching network components. Subsequently, [66] stated the design consideration for the impedance matching network and proposed the general type of impedance matching networks. Nevertheless, [67] presents a detailed analysis and design considerations for lumped (inductor and capacitor) matching networks. Lastly, [68] analyzed the multistage matching networks and provides the optimization parameters.

C. RF-DC RECTIFIER

In RF energy harvesting, the power received from the antenna is low in density, requiring boosting or multiplying of the received power in order to produce sufficient voltage [69]. Also, the power received is in AC voltage, thus, rectification is necessary to convert the AC voltage to a usable DC voltage. Therefore, the integration of an RF-DC rectifier is essential for the purpose of voltage multiplication and voltage rectification of the received RF power [70].

In short, RF-DC rectification includes two types which are half-wave rectification and full-wave rectification. A half-wave rectifier can be made by placing a single diode in series or in parallel with the output load, which is also known as the single-series rectifier [71] and single-shunt rectifier [72] respectively. However, research from [73] shows that the half-wave rectifier produces lower efficiency as compared to the full-wave rectifier. On the other hand, there are three types of full-wave rectifiers which are the Cockcroft-Walton rectifier, Dickson-type rectifier, and cross-coupled differential-drive (CCDD) rectifier. The Cockcroft-Walton rectifier is also known as the Greinacher rectifier or Villard rectifier [74]. In this topology, the coupling capacitors for multiple stages are connected in series as shown in Fig. 5(a), leading to a significant voltage drop per stage [74]. To reduce the voltage drop, the coupling capacitors are placed in parallel for multiple stages as shown in Fig. 5(b), which is known as the Dickson-type rectifier [75]. The Dickson-type rectifier is the enhanced version of the Cockcroft-Walton topology. Unlike the Cockcroft-Walton topology which is typically used for the high-voltage application, the Dickson-type topology is suitable for low-voltage applications [9].

In that case, the two main rectifier topologies in the RFEH system are the Dickson-type rectifier and the CCDD-type rectifier. Both topologies differ in the rectification approach. In short, there are two main differences. First, a Dickson-type rectifier requires single-ended input while a CCDD-type rectifier requires differential input. Second, a Dickson-type rectifier uses the transistors as a diode while a CCDD-type rectifier uses the transistors as the switch. There are three common indicators to evaluate the performance of the rectifiers which are sensitivity, PCE, and PDR.

The sensitivity in dBm is defined as the minimum input power required for the circuit to generate a certain amount of DC output. The common DC value in evaluating the sensitivity is 1V DC output [9]. The sensitivity of the rectifier determines the lowest RF power density applied to the input of the RFEH system for proper operation in a given environment. The sensitivity is defined as:

$$P_{dBm} = 10 \log_{10} P_{mW} \tag{8}$$

where $\boldsymbol{P_{dBm}}$ is the rectifier's sensitivity expressed in dBm and $\boldsymbol{P_{mW}}$ is the rectifier's received power expressed in milliwatts.

The PCE measures the efficiency of the RFEH system through the ratio of the DC output power to the rectifier's input received power [76].

$$\eta_{REC} = \frac{P_{DC}}{P_{REC}} \tag{9}$$

where $\boldsymbol{\eta_{REC}}$ is the rectifier's PCE, $\boldsymbol{P_{DC}}$ is the DC power at output and $\boldsymbol{P_{REC}}$ is the rectifier's received power.

The PDR of the rectifier is determined by the continual range of the input received power at which the PCE of the rectifier maintains its value above a certain percentage. The common percentage of determining the PDR is above 20% [39], [19]. The PDR defines the output stability of the system in deciding whether the RFEH system is capable of continuously maintaining the efficiency in generating the output voltage.

In reference to the indicator parameters as above, it is desirable to strive for high sensitivity, high PCE, and wide PDR. The output parameter for the RFEH system is the DC output voltage. By stacking or cascading the stage of rectifiers, the low RF input voltage can be multiplied to produce the desired DC output voltage.

A common single-stage Dickson-type rectifier consists of two diode-connected transistors, $\boldsymbol{M_1}$ and $\boldsymbol{M_2}$ and two capacitors, $\boldsymbol{C_1}$ and $\boldsymbol{C_2}$, as shown in Fig. 6(a).

During the negative cycle, the transistor $\boldsymbol{M_1}$ is on while the transistor $\boldsymbol{M_2}$ is off. Thus, the capacitor $\boldsymbol{C_1}$ charges up to a voltage value of:

$$V_{C1} = V_P - V_{TH1} \tag{10}$$

where $\boldsymbol{V_P}$ is the peak amplitude of RF input and $\boldsymbol{V_{TH1}}$ is the threshold voltage of the transistor $\boldsymbol{M_1}$.

During the positive cycle, the transistor $\boldsymbol{M_1}$ is off while the transistor $\boldsymbol{M_2}$ is on. At this point, the capacitor $\boldsymbol{C_2}$ charges up to a voltage value of:

$$V_{C2} = V_P + V_{C1} V_{TH2} \tag{11}$$

or

$$V_{C2} = V_P + V_{C1} V_{TH1} - V_{TH2} \tag{12}$$

where V_{TH2} is the threshold voltage of the transistor M_2.

The single-stage output voltage ($V_{OUT,1}$) is the voltage of the capacitor C_2, thus, the expression of a single-stage Dickson-type rectifier can be written as:

$$V_{OUT,1} = 2V_P - V_{TH1} - V_{TH2} \tag{13}$$

The multi-stage output voltage ($V_{OUT,n}$) of a Dickson-type rectifier can be expressed as:

$$V_{OUT,n} = n \times V_{OUT,1} \tag{14}$$

where n is the number of cascaded stages.

Dickson-type rectifier produces a high voltage at the cost of poor sensitivity and lowers PCE [8], [9], [77]. As observed from (10), the output voltage of the Dickson-type rectifier suffers from the inevitable drop of V_{TH}. When it is required to produce higher DC voltage, more stages are essential, resulting in more voltage drop as described in (14) which eventually degrades the sensitivity and PCE [78]. To increase the performance of Dickson-type rectifiers, research on compensation or cancellation of V_{TH} has been conducted. The first technique is through self V_{TH} compensation (SVC), which can be achieved by interconnecting the terminals of transistors of the same stage. References [79] and [80] proposed the SVC method where the NMOS gate terminal connects to the output terminal while the PMOS gate terminal connects to the ground. This method achieves a peak PCE of 32% at a low input power of −10 dBm. The second technique is the inter-stage V_{TH} compensation (ISVC) by connecting the gate terminal of the transistors to the subsequent stage [81], [82], achieving a high sensitivity of −19 dBm and −20 dBm. Subsequently, the third technique is the internal V_{TH} compensation (IVC) by adding capacitors or circuits at the output to bias the gate terminal of transistors. A passive current-mirror bias circuit to cancel out the V_{TH} drop was proposed by [83] and [84], where a peak PCE of 36.6% have been achieved. Alternatively, [85] proposed an IVC alike method - the floating-gate technique, which reports an operation condition as low as −22.6 dBm. However, the floating-gate technique requires a pre-charge phase which is inconvenient and unattractive [86]. Lastly, there is also work reported on external V_{TH} compensation (EVC) achieved by integrating external power supply or external control such as external clocking switched-capacitor circuit, where a sensitivity of −14 dBm has been recorded [87]. However, compensation of V_{TH} usually comes with the trade-off in reverse leakage current. To offset the effect of reverse leakage current, [88], [89] proposed an adaptive threshold voltage compensation scheme while [90] investigated an optimization for bias voltage (V_C).

The CCDD rectifier is a topology derived from the full-wave diode-bridge rectifier. Commonly CCDD-type rectifier consists of two NMOS transistors (M_{N1}, M_{N2}), two PMOS transistors (M_{P1}, M_{P2}) and two coupling capacitors (C_{C1}, C_{C2}), as shown in Fig. 6(b). The integration of coupling capacitors in the circuit allows the AC RF input signal to pass through while blocking the DC charges.

During the negative cycle, M_{P2} and M_{N1} turns on while M_{P1} and M_{N2} turns off. At this point, it creates a complete loop for the rectification. During the positive cycle, M_{P2} and M_{N1} turns off while M_{P1} and M_{N2} turns on. In this case, the complete circuit loop with the same current direction respective to the negative cycle occurs.

CCDD-type rectifier achieves high peak PCE but narrow PDR [8], [9], [77]. This transpires as the CCDD-type rectifier suffers from unwanted reverse leakage current at high RF input [17]. When the number of stages increases, the output voltage may be higher than the input voltage. In this case, the reverse leakage current becomes severe, degrading the overall performance. To increase the performance of CCDD-type rectifier, research in eliminating or lowering the effect of reverse leakage current have been initiated. There are two main approaches: to detect and provide the counter solution to the high reverse leakage current or to build a high resilience circuit that is capable to withstand the effect of reverse leakage current. For the detection and counter solution, [91] and [92] proposed a feedback network to detect the strength of reverse current leakage and control the gate biasing of the transistors, where a peak PCE of 65% is achieved. In the second approach, [24] and [93] proposed complementary MOSFET with the aid of thick-oxide MOSFET to reduce the reverse leakage current, where a peak PCE of 75.2% has been reported. Subsequently, [94] and [95] proposed the integration of bootstrapping capacitors to minimize the leakage current effect. An 80% and 87% peak PCE have been recorded from the two projects, respectively.

In comparison to the two topologies, additional consideration should be accounted for in making the selection. The number of transistors required for the two topologies is different. A single-stage Dickson-type rectifier requires two transistors, while a single-stage CCDD-type rectifier requires four transistors. With the same dimension of the transistor, the transistor count of the CCDD-type rectifier doubles in comparison to the Dickson-type rectifier, with the penalty of increased area consumption. However, a single CCDD-type rectifier may achieve a higher PCE than the Dickson-type rectifier. Thus, the CCDD-type rectifier could potentially achieve the same PCE as the Dickson-type rectifier by comparatively adopting fewer stages, thus requiring a smaller area.

IV. MULTIBAND RFEH FRONT-END CIRCUITRY

Similar to the typical RFEH front-end system, the multiband RFEH front-end system consists of three main components, which are the multiband antenna, multiband impedance matching network and multiband rectifier. There are two main challenges in designing the multiband RFEH front-end circuit. The first challenge is that the front-end system must be capable in harvesting multiple frequency from the ambient environment. To cope with this, multiband antenna designs are needed.

The design challenge is also foreseen due to the non-linear characteristics of the rectifier [96], [97]. The rectifier is a non-linear device where the impedance varies respectively to the change in the operational frequency. In this case, a multiband or wide band impedance matching network is necessary to reduce the reflected power loss. Various impedance-matching networks have been proposed to harvest single-band frequency [98], [99], [100]. However, in the context of multiband RFEH systems, the single-band impedance matching network, which is initially targeted to match a single frequency, will produce significant reflection loss due to the impedance mismatch at a non-matching frequency. The working principle of the RF-DC rectification process is the same as with the single-band or multiband RFEH systems.

A. MULTIBAND RADIO FREQUENCIES

To design a multiband RF energy harvester, the first step is the selection of the targeted harvesting frequency. Referring to Fig. 2, 433 MHz, 900 MHz, 1.8 GHz, and 2.4 GHz are the four most commonly harvested center frequencies due to their density of use, leading to high signal strength. However, depending on the location and condition, the preferred frequency may have a relatively higher signal strength. In addition, there is also another potential harvesting frequency, such as 875 MHz, 1.9 GHz, and 2.5 GHz. In summary, the multiband RF is usually selected from the five listed center frequencies as highlighted above with a tolerable range.

However, a hidden trend can be observed by observing the improvement of GSM 2G, UMTS 3G, LTE 4G to 5G NR, where the preferred frequency increases from around 900 MHz to the current widely used 5G frequency of around 4 GHz. The current highest 5G frequency can be up to around 50 GHz. Therefore, this outlays a considerable gap of novelty to be discovered.

B. MULTIBAND RF RECEIVER ANTENNA

Antennas with multiband features can be designed easily by implementing multiple single-band antenna designs (MA) to harvest multiple frequencies simultaneously, as shown in Fig. 7(a). The example of the single-band antenna can be referred from Section III. However, such designs usually require a larger area. Therefore, a single antenna design with a multiband feature (SA) has been proposed.

A single antenna with the multiband feature can be classified into two categories: multi-narrowband or broadband design. The multi-narrowband antenna is designed to precisely create resonance at the desired frequency to harvest multiple frequencies with minimal losses, as shown in Fig. 7(b). On the contrary, the broadband antenna is designed to create a wide resonance covering all the desired frequencies to achieve multiband harvesting, as shown in Fig. 7(c).

Designing a wide lossless region for broadband antenna has its pros and cons. The advantage is that the wide broadband approach has higher adaptability compared to the multi-narrowband approach due to broad exposure to ambient frequency. However, the trade-off of using a broadband antenna is that the reflection loss is higher than the multi-narrowband antenna. This is because narrowband antennas can be optimized to harvest a specific frequency band. Moreover, the broadband approach has difficulty in producing an adequate wide region for two frequencies that are far apart, such as 900 MHz and 2.4 GHz. Therefore, the selection of an antenna may depend on different application scenarios.

For multi-narrowband harvesting of 900 MHz and 1.8 GHz, [101] proposed a dual-band second monopole antenna with the respective measured gain of 1.8 dBi and 2.06 dBi. The size of the proposed antenna is 9600 mm^2. To miniaturize the antenna size, [102] proposed a dual-band inverted-L (IL) shaped monopole antenna which is eight times smaller than the dual-band second monopole antenna with a size of 1200mm^2. As a trade-off, the proposed design comes with a lower gain of 1.46 dBi and 1.91 dBi at 900 MHz and 1.8 GHz respectively. Subsequently, [103] proposed a 2500mm^2 dual-band monopole antenna design. This design has recorded the highest gain of 2.36 dBi among the three monopole designs. Other than dual-band harvesting from 900 MHz and 1.8 GHz, [104] proposed a dual-band loop antenna to harvest from 915 MHz and an uncommon frequency of 945 MHz. The design measures a gain of 1.3 dBi for both of the bands. The work [105] proposed a dual-band slot loaded folded dipole antenna to harvest from 915 MHz and 2.45 GHz with a measured gain of 1.87 dBi and 4.18 dBi respectively.

There are also several proposed design to harvest from tri-band and quad-band. Reference [106] proposed a tri-band slotted/slitted antenna to harvest energy from 2 GHz, 2.5 GHz and 3.5 GHz. The measured gain for the tri-band are 7 dBi, 5.5 dBi and 9.2 dBi respectively. To realise tri-band harvesting, the planar implementation requires a large size of 25600 mm^2. Comparatively reporting with the same size of 25600 mm^2, [107] proposed a quad-band bow-tie antenna to harvest from 850 MHz, 1.8 GHz, 2.18 GHz, and 2.4 GHz. The highest measured gain for this quad-band design is 4.82 dBi at 2.4 GHz. Improvising from [80] and [108] proposed a quad-band fork-shaped antenna to harvest from 950 MHz, 1.81 GHz, 2.42 GHz, and 2.9 GHz. The design recorded the highest measured gain of 7.6 dBi for 2.42 GHz. However, the implementation requires a larger size of 48400 mm^2.

For broadband harvesting, [109] introduced a 64-element dual-circularly-polarized spiral-shaped antenna array with a broad harvesting frequency from 2 GHz to 18 GHz. Due to the presence of 64 spiral elements array, the realization of this design requires a comparatively large size of 33300 mm^2. On the other hand, [110] proposed a 1×4 Quasi-Yagi antenna array that produces a lossless broadband region that includes the desired frequency of 1.8 GHz and 2.1 GHz. The work measures a gain of 13.3 dBi, which is the highest among the reviewed design. However, the bottleneck of this solution is in the large size of 38000 mm^2.

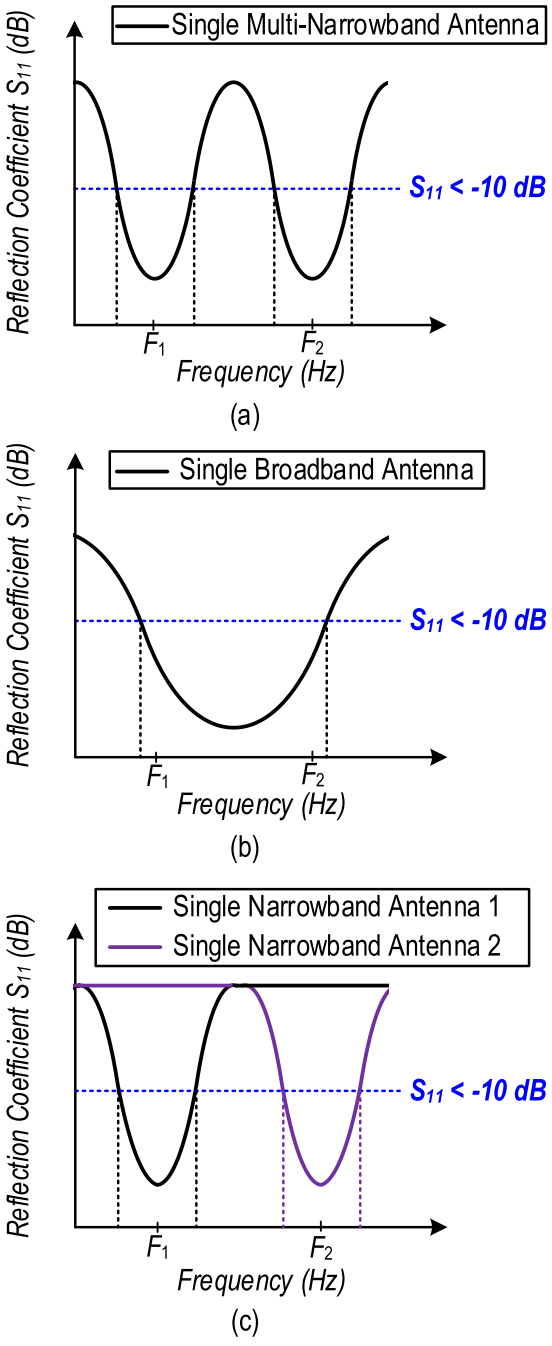

FIGURE 7. General type of multiband antenna: (a) Multiple single-band antenna. (b) Single multi-narrowband antenna. (c) Single broadband antenna.

To minimize the size, [111] proposed a planar cross dipole dual-polarized antenna while [112] proposed a bent triangular omnidirectional antenna to produce a lossless broadband region to harvest from their desired dual-band frequency respectively. Both works report a smaller size of 4900 mm^2 and 7708 mm^2 correspondingly. However, their respective measured gains are lesser than [110], which are 2.5 dBi for 1.8 GHz and 3.95 dBi for 2.5 GHz as in [111] and 2 dBi for both 950 MHz and 1.85 GHz in [112].

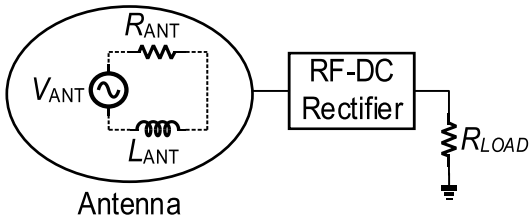

FIGURE 8. General IMN-less rectenna design.

C. MULTIBAND IMPEDANCE MATCHING NETWORK

The impedance matching network is essential in the RFEH front-end system to eliminate the unwanted impedance mismatch reflection loss. In the implementation of an IMN-less rectenna design as shown in Fig. 8, the need for the IMN network is eliminated. IMN-less rectenna is a device with a customized antenna and rectifier to convert RF energy into DC voltage output. References [113] and [114] proposed a tunable rectenna capable of tuning the antenna's impedance and matching it conjugately with the impedance of the rectifier. In this design, the impedance-matching network block can be excluded from the multiband circuit. However, the integration of a rectenna in the multiband RFEH system has its downsides. The antenna has to be specially customized, contributing to higher cost, complexity, and low adaptability.

In brief, this section lists the state-of-the-art multiband IMN. As the harvesting frequency and the impedance of the rectifier are completely different, the size of the multiband IMN designs cannot be used to indicate the performance of the IMN designs. Therefore, to ensure fairness in comparison, the reflection loss $\boldsymbol{S_{11,dB}}$ will be the only indicator in determining the performance of the design. As highlighted, the multiband IMN design with $\boldsymbol{S_{11,dB}}$ less than -10 dB for both bands will be considered as matched.

Abstaining the need in customizing the antenna, RFEH system researchers proposed the use of a transmission line (TL) or microstrip line [115], [116], [117], [118], [119], [120] as the impedance matching network and integrates the diode as the rectifier to build a simple multiband RFEH system, as shown in Fig. 9. Schottky diodes are the preferred selection for the rectifier in this method [121], [122]. In general, the transmission line impedance matching network can be classified into single branch matching networks (SBMN) or multiple branch matching networks (MBMN). Both methodologies differ in the number of branches required for multiband matching.

For the SBMN implementation, several designs have been proposed resonating at 915 MHz and 2.45 GHz. Reference [115] proposed a series combination of Pi-matching TL network and L-matching TL network. This design requires a total of five TL segments with an approximate average segment dimension of 1.3mm/29.3mm (width/length) and an approximate matching network circumference of 295mm. To minimize the size, [116] proposed a novel stepped impedance stub matching network built from three TL

segments with an approximate average segment dimension of 1.3mm/12.2mm and an approximate matching network circumference of 76mm. Smaller TL segment dimension leads to an improvement in size optimization. In addition, [117] reported a three-TL segment single-stage T-matching TL network design with an approximate average segment dimension of 0.7mm/26.5mm and an approximate matching network circumference of 147mm. The design outstands for its smallest width of the TL segment. All three SBMN designs recorded $S_{11,dB}$ of −40 dB, −22.5 dB and −25 dB respectively, complying to the matching condition of less than −10 dB.

In addition, several MBMN designs have been reported. Reference [118] proposed a dual-branch T-junction coupled line matching network to harvest energy from a dual band of 915 MHz and 2.45 GHz. Both branches consist of three TL segments, leading to a total of six TL segments. The approximate average segment dimension is 1.9mm/20.9mm. Respective of a total of six TL segments, the design requires a bigger approximate matching network circumference of 299mm as a trade-off. Subsequently, [119] proposed a triple branch impedance matching network built from a single radial stub, a single short stub, and a TL segment at each branch, contributing to a total of nine TL segments. This design comes with a small approximate average segment dimension of 3.4mm/12.5mm. However, the use of nine TL segments contributes to a larger value of 219mm for the approximate matching network circumference. Both the multiple branch design measures a $S_{11,dB}$ of −20 dB and −21 dB respectively.

In brief, the TL matching network can achieve a matched condition between the antenna and the rectifier. In addition, the TL matching network is known to have greater efficiency in impedance matching of frequencies higher than 2.6 GHz compared to the LC-based matching network [123]. From the research work [123], the insertion loss for the TL matching network and LC-based matching network are benchmarked, and the result shows that the insertion loss for the TL matching network and LC-based matching network is similar in the frequency of 2.6 GHz and less. Beyond the frequency of 2.6 GHz, the TL matching network has a significant advantage over the LC-based matching network and can achieve a lesser insertion loss. However, most of the congested harvesting frequencies, are lower than 2.6 GHz, concluding that the use of a TL matching network is less significant. Furthermore, the downside of using the TL matching network is the larger required size due to the off-chip PCB integration.

Apart from the off-chip PCB approach of rectenna, stripline, and microstrip line implementation, the CMOS approach adopts passive components such as resistor, inductor, capacitor, or transformer in designing the multiband impedance matching network.

A low-loss CMOS multiband RFEH system is realized through the narrowband approach [70], [124], [125], [126], [127], [128], [129], [130], [131], [132], [133], [134].

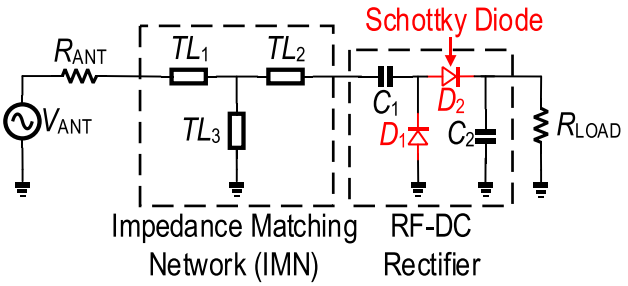

FIGURE 9. Transmission line impedance matching network.

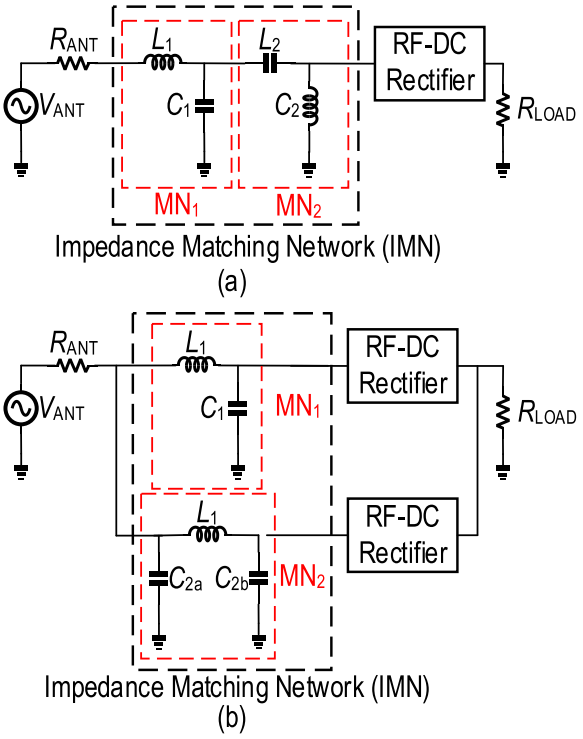

FIGURE 10. Dual-band: (a) Single branch matching network. (b) Multiple branch matching network.

The narrowband impedance matching network focuses on creating a one-to-one matching scenario. A one-to-one matching scenario can be further classified as a single branch matching network and multiple branch matching networks. Fig. 10(a) and Fig. 10(b) show an example of on-chip SBMN and MBMN. The matching networks differ mainly in size and complexity.

The CMOS-based SBMN focuses on a series combination of several matching networks, such as the implementation of two L-matching networks in series to match with dual-band [124]. Besides the combination of series networks, SBMN may also employ a tunable approach, as shown in Fig. 11; however, this requires an extra loop or circuit to release the control signal, increasing the circuit complexity and uncertainty. Alternately, the CMOS-based MBMN focuses on a parallel combination of several single-band matching networks. For instance, a dual-band matching network can be built from two single-band matching networks, where each

single-band matching network is responsible to match with a single frequency.

In reference to SBMN, [124] proposed a fully on-chip series double L-matching network produce two resonant frequencies at 915 MHz and 2.4 GHz. The reflection loss, $S_{11,dB}$ are −37 dB and −33 dB for the dual frequency respectively. The work [125] proposed an on-chip tunable single L-matching network. Adopting a tunable LC matching network, the $S_{11,dB}$ reflection loss can be as low as −36 dB and −40 dB at 900 MHz and 1.9 GHz respectively. Alternatively, [126] proposed a tunable 4-bit capacitor bank based broadband impedance matching network to match with a frequency range between 700 MHz to 900 MHz. The work reported a reflection loss $S_{11,dB}$ of less than −10 dB in the defined frequency range. In brief, on-chip design are capable to maintain the perfect matched condition. However, on-chip impedance matching network suffers from low Q-factor for the inductor and capacitor due to high losses in the substrate [135]. To address this issue, several work in employing off-chip inductor and capacitor are proposed [70], [127], [128], [129], [130], [131], [132], [133], [134]. Reference [127] proposed a novel impedance matching network with a 1:100 transformer and a single LC matching network. Reference [128] proposed two external SMD inductors as the matching network and fine-tuned it to match at dual frequencies of 900 MHz and 1.8 GHz. Reference [129] proposed a 900 MHz and 2.4 GHz dual-band impedance matching network built from two L-matching networks. Due to the differential RF input, a total of four off-chip inductors and capacitors are used. The reflection loss, $S_{11,dB}$ is measured as −15.8 dB and −17.8 dB at 900MHz and 2.4GHz, respectively. Subsequently, [130] recorded a reflection loss of −24.8 dB and −23.5 dB for 902 MHz and 2.45 GHz respectively using an off-chip matching.

In reference to on-chip MBMN design, [131] proposed a dual-parallel L-matching network to match with 915 MHz and 1.85 GHz respectively. The work [134] proposed a Pi-matching network to match at 915 MHz and an L-matching to match at 2.4 GHz. This work reported a reflection loss $S_{11,dB}$ of −16 dB and −20 dB for both of the bands. Additionally, there are also some reported design on off-chip MBMN, such as dual-parallel branch design [133] and tri-parallel branch design [70], [132].

D. MULTIBAND RF-DC RECTIFIER

Unlike the single-band RFEH system, the multiband RFEH system aims to harvest from multiple frequencies, resulting in multi-branch input power at the rectifier block. Concurrently, a multi-branch rectifier (MBR) can be proposed where each branch is individually responsible for processing a single branch of input power. The output of each branch combines to form a larger output [70], [134]. However, MBR encounters current leakage between the branch due to the inherent potential difference. In addressing this setback, [131] proposed a diode summation network and switch summation network to control the leakage current in between the branch, hence, improving the output summation voltage. Moreover, [136] introduced an intelligent shortcut switching summation network that can improve the power summation performance at higher input power. Furthermore, [137] analyzed and introduced a new connection for the diode summation network by connecting a single output node to all other output nodes with the usage of a properly oriented and low leakage diode. As simplified in Fig. 14(a) and (c), the diode or switch summation network is implemented as a power combiner to allow the summation of power for a multiband RFEH front-end system [131], [136], [137].

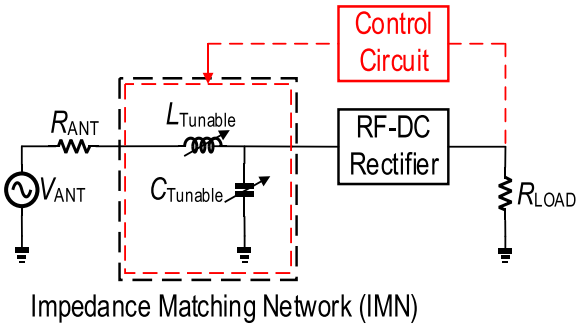

FIGURE 11. Multiband tunable impedance matching network design.

Alternately, the multiband RFEH system could combine the input power at an early stage, leading to a single branch input power to the rectifier block. The implementation promotes a single-branch rectifier (SBR) realization. An SBR design benefits the Dickson-type which suffers from poor sensitivity due to the presence of threshold voltage. With the aid of high input power, the threshold voltage can be easily overcome [138].

However, the CCDD rectifier suffers from reverse leakage current, especially at high input power. Thus, the SBR design will worsen the reverse leakage current of the CCDD-type rectifier, leading to a drop in the output voltage [139]. In addressing this bottleneck, methods to eliminate the reverse leakage current have been presented in Section III. These methods can be adopted for multiband energy harvesting schemes. For instance, [128], [131], and [134] proposed a multiband RF-DC rectifier with threshold voltage self-compensation to reduce the reverse leakage current. The proposed technique would improve the performance of the CCDD-type rectifier for multiband energy harvesting.

V. MULTIBAND RFEH FRONT-END SYSTEM CIRCUIT INTEGRATION

The rectenna design, as in [113], [114], and [140] will not be considered in this part. The reason is that the rectenna design requires a specially customized antenna that will not fit with the standard sensor nodes and IoT solution available in the market designed to connect with a standard 50Ω antenna.

A multiband RFEH front-end system will use the combination of the multiband circuitry listed in Section IV. There are two initial types of multiband antenna design (SA and MA), two types of multiband IMN design (SBMN

TABLE 1. Multiband antenna design with size and gain.

Ref	Frequency (MHz)	Types	Antenna	Size (mm^2)	Gain (dBi)
[101]	900/1800	Dual	Second Monopole	9600	1.8/2.06
[102]	900/1800	Dual	Inverted-L (IL) Shaped Monopole	1200	1.46/1.91
[103]	900/1800	Dual	Monopole	2500	0.62/2.36
[104]	915/945	Dual	Loop	9273.69	1.3/1.3
[105]	915/2450	Dual	Slot Loaded Folded Dipole	3600	1.87/4.18
[106]	2000/2500/3500	Tri	Slotted/slitted	25600	7/5.5/9.2
[107]	850/1810/2180/2400	Quad	Bow-tie	25600	3.95/4.45/4.42/4.82
[108]	950/1810/2420/2900	Quad	Fork-shaped	48400	3.2/3.7/7.6/2.9
[109]	2000-18000	Broad	64-element Dual-circularly-polarized Spiral Array	33300	n.a.
[110]	1800/2100	Broad	1 x 4 Quasi-Yagi Antenna Array	38000	10.9/13.3
[111]	1800/2500	Broad	Planar Cross Dipole Dual-polarized	4900	2.5/3.95
[112]	950/1850	Broad	Bent Triangular Omnidirectional	7708	2/2

TABLE 2. Multiband impedance matching network design.

Ref	Freq (MHz)	Tech	IMN Method	$S_{11,dB}$
[115]	915/2450	PCB	Pi-matching and L-matching in series	-40, -40 *
[116]	915/2450	PCB	T-matching	-25, -20
[117]	915/2450	PCB	Single-stage T-matching	-24.4, -27.5
[118]	915/2450	PCB	T-junction and Dual-branch coupled line	-18, -22 *
[119]	900/1800/2450	PCB	Tri-branch radial stub, short stub	-17, -25, -21
[124]	915/2450	CMOS 180nm	Two L-matching in series	-37, -33
[125]	900/1900	CMOS 130nm	Tunable L-matching	-40, -36
[126]	700-900	CMOS 130nm	Tunable 4-bit Capacitor Bank	-36, -22, -10
[127]	900/2400	CMOS 180nm	Adaptive L-matching	-15.8, 17.8
[130]	902/2.45	CMOS 180nm	Off-chip matching	-24.8, -23.5
[134]	915/2400	CMOS 180nm	L-matching and Pi-matching in parallel	-26, -20

*Simulation results

TABLE 3. Multiband RF-DC rectifier design.

Ref	Rectifier Type	Transistor/Diode	Number of Branches	Number of Stages	Rectifier Remarks
[70]	CCDD	LVT MOSFET	3	3	Conventional
[130]	CCDD	MOSFET	1	5	Threshold Voltage Auto Cancellation
[131]	CCDD	LVT MOSFET	2	10	Threshold Voltage Self-compensation
[132]	CCDD	MOSFET	2	4	Hybrid Threshold Voltage Self-compensation
[133]	Dickson	MOSFET	1	1	Internal Threshold Voltage Compensation
[116]	Half Wave	BAT15-03W	1	1	Schottky Diode
[117]	Full wave	HSMS 2862	1	1	Schottky Diode
[118]	Full wave	HSMS 2822 HSMS 2852	2	1	Schottky Diode
[120]	Half Wave	HSMS-2850 HSMS-2860	1	1	Schottky Diode

and MBMN), and two types of multiband rectifier design (SBR and MBR). Therefore, eight different multiband front-end system combinations are possibly realized as shown in Fig. 12.

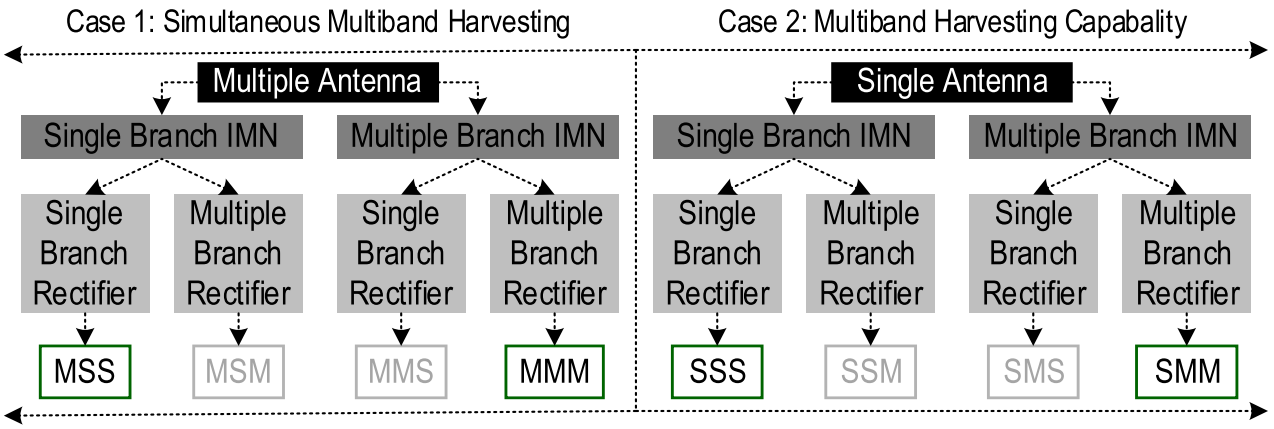

FIGURE 12. Multiband front-end system combinations (8 types).

TABLE 4. The sensitivity and power dynamic range (PDR) performance of second case designs.

Ref	Frequency (MHz)	Sensitivity @ 1V			Power Dynamic Range (PDR) @ > 20%		
		Single-band	Multiband	Improvement	Single-band	Multiband	Improvement
[124]	915	-2 dBm	-2 dBm	-	5 dB (-2 dB to 3 dB)	7 dB (-4 dB to 3 dB)	2 dB
	2450	-0.5 dBm		1.5 dBm	6 dB (-4 dB to -2 dB)		1 dB
[130]	902	-3 dBm	-3 dBm	-	19 dB (-9 dB to 10 dB)	20 dB (-9 dB to 11 dB)	1 dB
	2450	2 dBm		5 dBm	13 dB (2 dB to 11 dB)		7 dB
[134]	915	-19.8 dBm	-19.8 dBm	-	31 dB * (-19 dB to -12 dB)	31.3 dB * (-19 dB to -12.3 dB)	0.3 dB
	2400	-18.5 dBm		1.3 dBm	28.7 dB * (-16.4 dB to -12.3 dB)		2.3 dB

* PDR > 10%

TABLE 5. Output voltage for each circuit type.

Types	V_{IN} to Rectifier Block (each branch)	Number of Rectifier Stage (each branch)	V_{OUT} Formula
SSS	1	N	$2(N \times V_{\mathrm{IN,REC}}) - Losses$
SMM	$\frac{1}{N_B}$	$\frac{N}{N_B}$	$\frac{2}{N_B}(N \times V_{\mathrm{IN,REC}}) - Losses$
MSS	N_B	N	$2N_B(N \times V_{\mathrm{IN,REC}}) - Losses$
MMM	N_B	$\frac{N}{N_B}$	$2(N \times V_{\mathrm{IN,REC}}) - Losses$

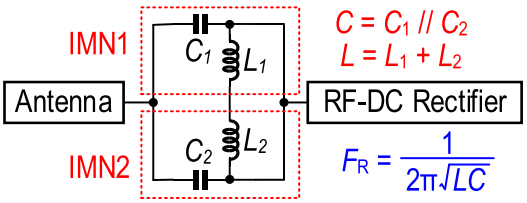

FIGURE 13. Impedance matching network problem.

From the eight combinations, two considerations have to be followed to avoid unwanted output voltage drop. The first consideration is in between the impedance matching network and the rectifier. Based on the rectifier cascading scheme analysis reported in [141], the output DC voltage is dependent on two main parameters which are the number of cascaded rectifier stages, and the rectifier input voltage:

$$V_{OUT} = 2N \times V_{IN,REC} - Losses \tag{15}$$

where V_{OUT} is the output voltage, $V_{IN,REC}$ is the input voltage to the rectifier, N is the number of cascaded rectifier stages, and the ***Losses*** which includes the threshold voltage losses and matching losses. Therefore, the SSM-type and MSM-type where SBMN connects with MBR divide

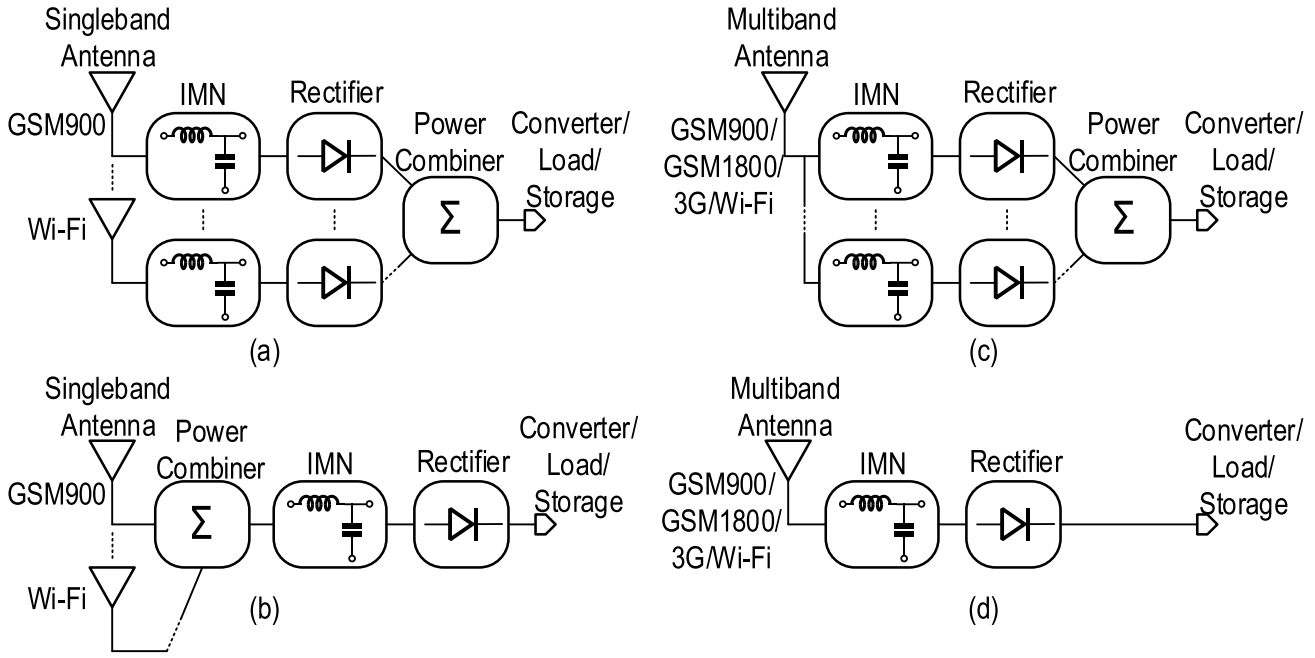

FIGURE 14. RFEH front-end system integration: (a) MMM-type. (b)MSS-type. (c) SMM-type. (d) SSS-type.

the input current to each branch of the rectifiers which directly results in the output current drop as given in (15). Assuming the SSM-type, the output voltage can be derived from [141]

$$V_{OUT,SSM} = N_B \left(\frac{2N}{N_B} \times \frac{V_{IN,REC}}{N_B} \right) - Losses \tag{16}$$

$$V_{OUT,SSM} = \frac{1}{2N_B} (N \times V_{IN,REC}) - Losses \tag{17}$$

where $V_{OUT,SSM}$ is the output voltage for the SSM-type and N_B is the number of rectifier branches. Comparing (15) and (17), the output DC voltage drops with a ratio of ($1/4N_B$). To compensate for this, more stages of rectifier at each branch are required, inevitably increasing the total size. The second consideration assumes MBMN connects to SBR, as shown in Fig. 13. This causes undesired impedance matching problems as the matching branch in MBMN are now parallel to each other. The inductance and capacitance for each branch are combined to form single inductance and single capacitance, leading to a match at a single frequency. Thus, the SA-MBMN-SBR (SMS-type) and MA-MBMN-SBR (MMS-type) are less favorable. From the two considerations, it concludes that the IMN and rectifier must have the same number of branches to avoid the division of rectifier input power and prevent the undesired matching problem.

Alternately, the remaining four combinations are used separately in two different cases. The first case utilizes the advantage of a multiband RFEH system with the ability to scavenge multiple input power from multiple frequencies simultaneously, which leads to higher output power. To harvest multiple frequencies concurrently, the system must consist of an MA design. With this regard, the potential options are the MA-MBMN-MBR (MMM-type) and MA-SBMN-SBR (MSS-type) as shown in Fig. 14(a) and Fig. 14(b) respectively. The former design sums up the output power from each rectifier branch, resulting in a larger single output power. The latter design sums up the received power from the antenna, leading to a larger single input power for the following IMN and rectifier. About these two circuit combinations, harvesting multiple frequencies simultaneously improves the output PCE [142], circuit sensitivity [70], and dynamic range [127], [132], [142]. Reference [142] reports an improvement of 8%, 18%, and 25% in PCE when combining the tri-band compared to the respective single band. Reference [70] reports a triple parallel branch RFEH front-end system using a 3-stage gate cross-coupled (FGCC) that produces a 4.6 dB enhancement in the sensitivity when combining three bands compared to a single band. On the other hand, [127], [132] reports a 30 dB wide operation range by summing the output from dual band from the RFEH front-end system.

Besides, the second case has the advantage of a multiband RFEH system with the ability to operate in multiple harvesting frequencies, leading to a wider harvesting system. Unlike the first case, the second case does not require harvesting multiple frequencies at the same time. In the absence of these constraints, the system can use the SA design. The potential options are the SA-MBMN-MBR (SMM-type) and SBMN-SBR (SSS-type) as shown in Fig. 14(c) and Fig. 14(d) respectively. By adopting the SSS-type [124], [130] and SMM-type [134], the circuit benefits in terms of sensitivity and dynamic range as shown in Table 4.

In brief, the four different combinations of topology in harvesting multiband frequency results in a dedicated output voltage formulation in reference to (15). The derivation is based on the assumption that the system is matched, with

TABLE 6. Multiband RFEH front-end circuit type with performance.

Ref.	Tech. (nm)	Freq. (MHz)	Circuit Type	Matching Network Topology	Rectifier Topology	Output Load	End-to-End Peak PCE	Sensitivity at 1V	End-to-End PDR
[70][a]	130	850 1900 2400	MMM	Off-chip LC matching	CCDD	100kΩ	70% @ -17 dBm 68% @ -17.2 dBm 66.2% @ -17.2 dBm 66.3% @ -23.2dBm [Tri]	-22.9 dBm @ 100kΩ [Tri]	30 dB*
[124][a]	180	915 2450	SSS	L-matching in series	Dickson	5kΩ 7kΩ	24.945% @ 2 dBm 24.404% @ 1 dBm	-1 dBm* @ 5kΩ	6 dB*
[125]	130	900 1900	SSS	Tunable L-matching[b]	CCDD	147kΩ	15.44% @ -4 dBm 26.33% @ -4 dBm	-14 dBm @ ∞Ω	16 dB
[127]	180	90 900	MSS	Off-Chip LC matching	CCDD	∞Ω	45%@ 5 dBm 55%@ 5 dBm	-25 dBm @ ∞Ω	n.a.
[129]	180	900 2400	SSS	L-matching in series[c]	CCDD	100kΩ	69.3% @ -12 dBm 64% @-12 dBm 67.1% @ -12 dBm [Dual]	-17 dBm @ 100kΩ	21 dB*
[130]	180	902 2450	SSS	Off-chip LC matching	Dickson	5kΩ	47% @ 1 dBm 27.1% @ 6 dBm	-3 dBm* @ 5kΩ	19 dB
[131][a]	130	915 1850	SMM	L-matching L-matching	CCDD	2.8MΩ	42.3%@ -16 dBm 44%@ -17 dBm 43.2% @ -18 dBm [Dual]	-33 dBm @ ∞Ω	9 dB*
[132]*	150	90 900 1800	MSS	Off-Chip LC matching	CCDD	∞Ω	55% @ 5 dBm 65% @ 5 dBm 60% @ 5 dBm	-25 dBm @ ∞Ω	n.a.
[134]	180	915 2400	SMM	L-matching Pi-matching	Dickson	1MΩ	21.8% @ -15 dBm 16.7% @ -15 dBm	-19.8 dBm @ 1MΩ -18.5 dBm @ 1MΩ	4 dB*
[116]	PCB	915 2450	SSS	L-matching (3 TL)	Half-wave	1.5kΩ	74% @ 9 dBm 73% @ 9 dBm	0 dBm* @ 1.5kΩ	30 dB*
[117]	PCB	915 2450	SSS	T-matching (3 TL)	Dickson	1.5kΩ	81.7% @ 12 dBm 73.1% @ 12 dBm	0 dBm* @ 1.5kΩ	24 dB*
[118]	PCB	915 2450	SMM	L-matching (3 TL) L-matching (2 TL)	Dickson	0.62kΩ 4.7kΩ	66% @ 30 dBm 58% @ 30 dBm	5 dBm* @ 0.62kΩ	53 dB*
[119]	PCB	900 1800 2450	SMM	Radial Stub, Short Stub, TL (Parallel)	Dickson	3.8kΩ	54% @ 4 dBm 51% @ 4 dBm 48% @ 4 dBm	-2.5 dBm @ 3.8kΩ	26 dB*
[142]	PCB	925 1820 2170	MSS	T-matching (5 TL) with two Stub	Half-wave	5kΩ	40% @ -10 dBm 30% @ -10 dBm 25% @ -10 dBm 50% @ -10 dBm [Tri]	-15 dBm* @ 5kΩ	17 dB*

[a] Simulation results [b] Manual control needed [c] Off-chip components needed * Estimated from figure

the matching loss neglected. In reference to Table 5, with the exact amount of rectifier stage, MSS-type obtains the highest output voltage due to multiple antennae that harvest multiple sources simultaneously, leading to the increase of input received power to the rectifier block. Subsequently, the SSS-type and MMM-type lead in the output voltage. The SSS-type with a single antenna limits the received power from a single source, leading to a slightly lower performance than the MSS-type. The MMM-type topology integrates multiple branches with the distributed amount of

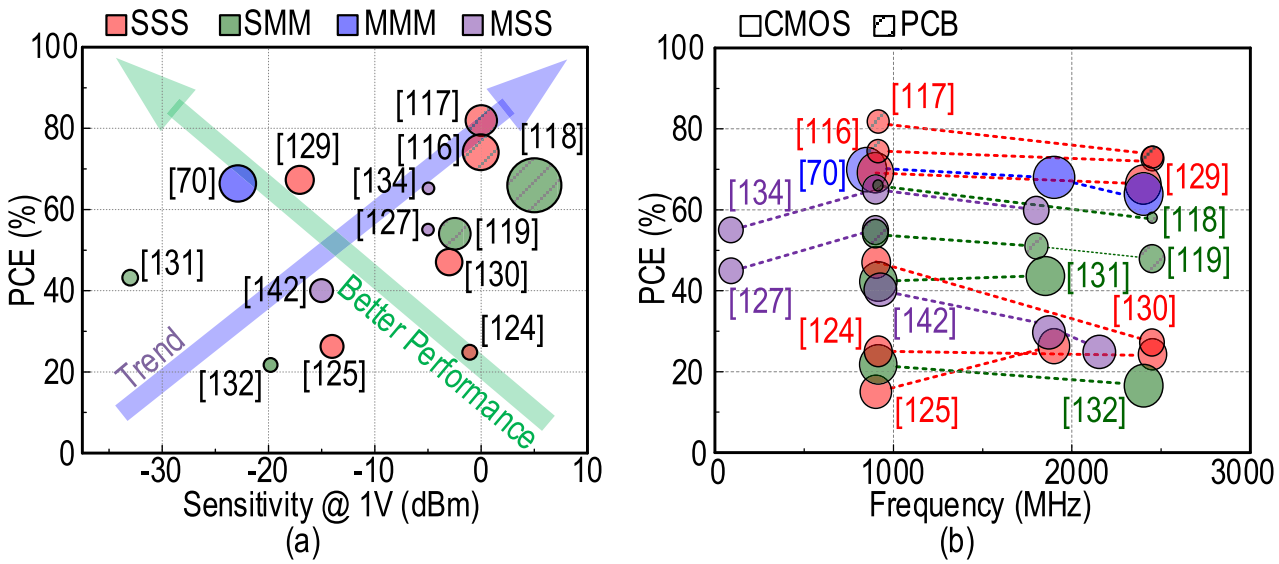

FIGURE 15. State-of-the-art multiband RFEH front-end system: (a) PCE versus Sensitivity. The size of the circle depicts the total PDR. (b) PCE versus Frequency. The size of the circle depicts the input power to attain peak PCE.

cascaded rectifier, thus degrading the boosting. However, the SSS-type and MMM-type topology achieves higher output voltage than the SMM-type. The SMM topology limits the input received power per time, further degrading the output voltage. However, it is worth noting that although the SSS-type and MMM-type topology exhibits the same output voltage expression, the design consideration is entirely different. The MMM-type multiband RFEH system has a similar architecture as in a combination of multiple single-band RFEH systems. On contrary, the SSS-type adopts an entirely new circuit architecture that only consists of single-branch multiband components. At the same time, the design approach for an SSS-type topology is completely different from the existing single-band system, thus wider research opportunity is established.

Based on Table 6, the four types of multiband RFEH front-end circuit enables good performance. The ideal performance matrix for the multiband RFEH front-end circuit tends to be a high PCE, high sensitivity, and wide power dynamic range. However, based on Fig. 15(a), most of the research work exhibits a trade-off between PCE, power dynamic range, and sensitivity. The work [117] shows a high PCE of 81.7% and a wide power dynamic range of 24 dB, but with a comparatively lower sensitivity at 0 dBm. Alternately, [131] has achieved good sensitivity of −33 dBm with the trade-off of lower PCE around 43.2%, simultaneously sacrificing the power dynamic range to 9 dB. In summary, good conduction leads to high sensitivity, however, at higher input power, PCE drops along with the power dynamic range due to the reverse current flow from the output to the input. Thus, the design trend emphasizes PCE enhancement. Nevertheless, sensitivity is a critical performance in the RFEH and is foreseen as a future research opportunity. Fig. 15(b) shows the PCE performance achieved by each harvesting frequency in the state-of-the-art multiband RFEH front-end system. Fig. 15(b) shows the research direction of prior works in the range of 90 MHz, 900 MHz, 1900 MHz, and 2400 MHz bands.

VI. CONCLUSION

This article reviews the recent state-of-the-art multiband RF energy harvesting front-end system, presented from the investigation of the RF survey in RF transmission and RF bands to the overview of the front-end architecture with the state-of-the-art multiband antenna design, multiband impedance matching network design, and multiband RF-DC rectifier design. The performance of prior state-of-the-art architecture is summarized and compared to investigate the advantage and disadvantages of different circuit architectures for multiband RFEH front-end systems. Subsequently, a section on the integration between the three core blocks of the multiband RFEH front-end has been discussed. In addition, critical considerations in designing a multiband RFEH front-end system are also provided to realize optimum performance targeting ultra-low power biomedical chips [13], [14], [15]. In summary, this article fills the research gap in the further advancement of multiband RF energy harvesting towards enhancing its performance through optimal circuit integration of the front-end system.

REFERENCES

[1] A. Adam, Y. Yusof, M. Iliyas, Y. Saif, and N. Hatem, "Review on manufacturing for advancement of industrial revolution 4.0," *Int. J. Integr. Eng.*, vol. 10, no. 5, pp. 1–6, 2018. [Online]. Available: https://publisher.uthm.edu.my/ojs/index.php/ijie/article/view/3013

[2] M. Grossi, "Energy harvesting strategies for wireless sensor networks and mobile devices: A review," *Electronics*, vol. 10, no. 6, p. 661, Mar. 2021, doi: 10.3390/electronics10060661.

[3] D. H. P. Kang, M. Chen, and O. A. Ogunseitan, "Potential environmental and human health impacts of rechargeable lithium batteries in electronic waste," *Environ. Sci. Technol.*, vol. 47, no. 10, pp. 5495–5503, Jan. 2013, doi: 10.1021/es400614y.

[4] H. Akinaga, "Recent advances and future prospects in energy harvesting technologies," *Jpn. J. Appl. Phys.*, vol. 59, no. 11, Nov. 2020, Art. no. 110201, doi: 10.35848/1347-4065/abbfa0.

[5] A. Satharasinghe, T. Hughes-Riley, and T. Dias, "A review of solar energy harvesting electronic textiles," *Sensors*, vol. 20, no. 20, p. 5938, Oct. 2020, doi: 10.3390/s20205938.

[6] J. Siang, M. H. Lim, and M. S. Leong, "Review of vibration-based energy harvesting technology: Mechanism and architectural approach," *Int. J. Energy Res.*, vol. 42, no. 5, pp. 1866–1893, Apr. 2018, doi: 10.1002/er.3986.

[7] J. Choi, I. Jung, and C.-Y. Kang, "A brief review of sound energy harvesting," *Nano Energy*, vol. 56, pp. 169–183, Feb. 2019, doi: 10.1016/j.nanoen.2018.11.036.

[8] A. C. C. Chun, H. Ramiah, and S. Mekhilef, "Wide power dynamic range CMOS RF-DC rectifier for RF energy harvesting system: A review," *IEEE Access*, vol. 10, pp. 23948–23963, 2022, doi: 10.1109/ACCESS.2022.3155240.

[9] G. Chong, H. Ramiah, J. Yin, J. Rajendran, W. R. Wong, P.-I. Mak, and R. P. Martins, "Ambient RF energy harvesting system: A review on integrated circuit design," *Anal. Integr. Circuits Signal Process.*, vol. 97, no. 3, pp. 515–531, Dec. 2018, doi: 10.1007/s10470-018-1320-4.

[10] R. P. Martins, P. Mak, C. Chan, J. Yin, Y. Zhu, Y. Chen, Y. Lu, M. Law, and S. Sin, "Bird's-eye view of analog and mixed-signal chips for the 21st century," *Int. J. Circuit Theory Appl.*, vol. 49, no. 3, pp. 746–761, Mar. 2021, doi: 10.1002/cta.2958.

[11] R. P. Martins, P.-I. Mak, S.-W. Sin, M.-K. Law, Y. Zhu, Y. Lu, J. Yin, C.-H. Chan, Y. Chen, K.-F. Un, M. Huang, M. Zhang, Y. Jiang, and W.-H. Yu, "Revisiting the frontiers of analog and mixed-signal integrated circuits architectures and techniques towards the future Internet of Everything (IoE) applications," *Found. Trends® Integr. Circuits Syst.*, vol. 1, nos. 2–3, pp. 72–216, 2021.

[12] M. H.-W. Loo, H. Ramiah, K.-M. Lei, C. C. Lim, N. S. Lai, P.-I. Mak, and R. P. Martins, "Fully-integrated timers for ultra-low-power Internet-of-Things nodes—Fundamentals and design techniques," *IEEE Access*, vol. 10, pp. 65936–65950, 2022, doi: 10.1109/ACCESS.2022.3183995.

[13] X. Feng, Y. Zhang, Y. Xuan, Z. Li, C. Yang, X. Xie, Y. Luo, X. Zhao, Y. Chen, and B. Zhao, "A square-wave stimulated DNA analyzer chip featuring 120 μW power consumption and simultaneous dual-frequency detection," *IEEE Trans. Circuits Syst. II, Exp. Briefs*, vol. 69, no. 10, pp. 4093–4097, Oct. 2022, doi: 10.1109/TCSII.2022.3184747.

[14] T.-H. Wang, Z. Li, B. Liang, Y. Cai, Z. Wang, C. Yang, Y. Luo, J. Sun, X. Ye, Y. Chen, and B. Zhao, "A power-harvesting CGM chiplet featuring silicon-based enzymatic glucose sensor," in *Proc. 44th Annu. Int. Conf. IEEE Eng. Med. Biol. Soc. (EMBC)*, Jul. 2022, pp. 4626–4630, doi: 10.1109/EMBC48229.2022.9871755.

[15] Z. Chang, C. Yang, Y. Zhang, Z. Li, T. Zheng, Y. Luo, S. Zhang, K. Xu, Y. Chen, G. Pan, and B. Zhao, "A battery-less crystal-less 49.8 μW neural-recording chip featuring two-tone RF power harvesting," in *Proc. IEEE Custom Integr. Circuits Conf. (CICC)*, Apr. 2022, pp. 1–2, doi: 10.1109/CICC53496.2022.9772792.

[16] A. K. Moghaddam, J. H. Chuah, H. Ramiah, J. Ahmadian, P.-I. Mak, and R. P. Martins, "A 73.9%-efficiency CMOS rectifier using a lower DC feeding (LDCF) self-body-biasing technique for far-field RF energy-harvesting systems," *IEEE Trans. Circuits Syst. I, Reg. Papers*, vol. 64, no. 4, pp. 992–1002, Apr. 2017, doi: 10.1109/TCSI.2016.2623821.

[17] G. Chong, H. Ramiah, J. Yin, J. Rajendran, W. R. Wong, P.-I. Mak, and R. P. Martins, "CMOS cross-coupled differential-drive rectifier in subthreshold operation for ambient RF energy harvesting—Model and analysis," *IEEE Trans. Circuits Syst. II, Exp. Briefs*, vol. 66, no. 12, pp. 1942–1946, Dec. 2019, doi: 10.1109/TCSII.2019.2895659.

[18] P. C. Kishore Kumar, H. Ramiah, M. Y. Ahmad, G. Chong, and J. Rajendran, "Analysis of a single-frequency multi-channel ambient RF energy harvesting in CMOS technology," in *Proc. IEEE Asia Pacific Conf. Circuits Syst. (APCCAS)*, Nov. 2019, pp. 97–100, doi: 10.1109/APCCAS47518.2019.8953107.

[19] A. Choo, H. Ramiah, K. K. P. Churchill, Y. Chen, S. Mekhilef, P.-I. Mak, and R. P. Martins, "A reconfigurable CMOS rectifier with 14-dB power dynamic range achieving >36-dB/mm^2 FoM for RF-based hybrid energy harvesting," *IEEE Trans. Very Large Scale Integr. (VLSI) Syst.*, vol. 30, no. 10, pp. 1533–1537, Oct. 2022, doi: 10.1109/TVLSI.2022.3189697.

[20] J. K. Yong, H. Ramiah, K. K. P. Churchill, G. Chong, S. Mekhilef, Y. Chen, P.-I. Mak, and R. P. Martins, "A 0.1-V V_{IN} subthreshold 3-stage dual-branch charge pump with 43.4% peak power conversion efficiency using advanced dynamic gate-bias," *IEEE Trans. Circuits Syst. II, Exp. Briefs*, vol. 69, no. 9, pp. 3929–3933, Sep. 2022, doi: 10.1109/TCSII.2022.3182344.

[21] K. K. Pakkirisami Churchill, H. Ramiah, G. Chong, M. Y. Ahmad, J. Yin, P.-I. Mak, and R. P. Martins, "A 0.15-V, 44.73% PCE charge pump with CMOS differential ring-VCO for energy harvesting systems," *Anal. Integr. Circuits Signal Process.*, vol. 111, no. 1, pp. 35–43, Apr. 2022, doi: 10.1007/s10470-021-01980-2.

[22] K. K. P. Churchill, H. Ramiah, G. Chong, Y. Chen, P.-I. Mak, and R. P. Martins, "A fully-integrated ambient RF energy harvesting system with 423-μW output power," *Sensors*, vol. 22, no. 12, p. 4415, Jun. 2022, doi: 10.3390/s22124415.

[23] T. Y. Chyan, H. Ramiah, S. F. W. M. Hatta, N. S. Lai, C.-C. Lim, Y. Chen, P.-I. Mak, and R. P. Martins, "Evaluation and perspective of analog low-dropout voltage regulators: A review," *IEEE Access*, vol. 10, pp. 114469–114489, 2022, doi: 10.1109/ACCESS.2022.3217919.

[24] M. Stoopman, S. Keyrouz, H. J. Visser, K. Philips, and W. A. Serdijn, "Co-design of a CMOS rectifier and small loop antenna for highly sensitive RF energy harvesters," *IEEE J. Solid-State Circuits*, vol. 49, no. 3, pp. 622–634, Mar. 2014, doi: 10.1109/JSSC.2014.2302793.

[25] M. A. Halimi, D. Surender, T. Khan, A. A. Kishk, and S. R. Rengarajan, "A multistepped transmission line matching strategy based triple-band rectifier for RFEH/WPT applications," *IEEE Microw. Wireless Compon. Lett.*, vol. 32, no. 8, pp. 1007–1010, Aug. 2022, doi: 10.1109/LMWC.2022.3162633.

[26] H. S. Vu, N. Nguyen, N. Ha-Van, C. Seo, and M. T. Le, "Multiband ambient RF energy harvesting for autonomous IoT devices," *IEEE Microw. Wireless Compon. Lett.*, vol. 30, no. 12, pp. 1189–1192, Dec. 2020, doi: 10.1109/LMWC.2020.3029869.

[27] D. Surender, T. Khan, F. A. Talukdar, and Y. M. M. Antar, "Rectenna design and development strategies for wireless applications: A review," *IEEE Antennas Propag. Mag.*, vol. 64, no. 5, pp. 16–29, Oct. 2022, doi: 10.1109/MAP.2021.3099722.

[28] M. Q. Dinh and M. T. Le, "Triplexer-based multiband rectenna for RF energy harvesting from 3G/4G and Wi-Fi," *IEEE Microw. Wireless Compon. Lett.*, vol. 31, no. 9, pp. 1094–1097, Sep. 2021, doi: 10.1109/LMWC.2021.3095074.

[29] S. Kim, R. Vyas, J. Bito, K. Niotaki, A. Collado, A. Georgiadis, and M. M. Tentzeris, "Ambient RF energy-harvesting technologies for self-sustainable standalone wireless sensor platforms," *Proc. IEEE*, vol. 102, no. 11, pp. 1649–1666, Oct. 2014, doi: 10.1109/JPROC.2014.2357031.

[30] K. T. Selvan and R. Janaswamy, "Fraunhofer and Fresnel distances: Unified derivation for aperture antennas," *IEEE Antennas Propag. Mag.*, vol. 59, no. 4, pp. 12–15, Aug. 2017, doi: 10.1109/MAP.2017.2706648.

[31] L. Cheng, W.-H. Ki, and C.-Y. Tsui, "A 6.78-MHz single-stage wireless power receiver using a 3-mode reconfigurable resonant regulating rectifier," *IEEE J. Solid-State Circuits*, vol. 52, no. 5, pp. 1412–1423, May 2017, doi: 10.1109/JSSC.2017.2657603.

[32] X. Lu, P. Wang, D. Niyato, D. I. Kim, and Z. Han, "Wireless networks with RF energy harvesting: A contemporary survey," *IEEE Commun. Surveys Tuts.*, vol. 17, no. 2, pp. 757–789, 2nd Quart., 2015, doi: 10.1109/COMST.2014.2368999.

[33] Y. Luo, L. Pu, G. Wang, and Y. Zhao, "RF energy harvesting wireless communications: RF environment, device hardware and practical issues," *Sensors*, vol. 19, no. 13, p. 3010, Jul. 2019, doi: 10.3390/s19133010.

[34] K. H. Joyner, M. J. Van Wyk, and J. T. Rowley, "National surveys of radiofrequency field strengths from radio base stations in Africa," *Radiat. Protection Dosimetry*, vol. 158, no. 3, pp. 251–262, Feb. 2014, doi: 10.1093/rpd/nct222.

[35] H. J. Visser, A. C. F. Reniers, and J. A. C. Theeuwes, "Ambient RF energy scavenging: GSM and WLAN power density measurements," in *Proc. 38th Eur. Microw. Conf.*, Oct. 2008, pp. 721–724, doi: 10.1109/EUMC.2008.4751554.

[36] X. Gu, L. Grauwin, D. Dousset, S. Hemour, and K. Wu, "Dynamic ambient RF energy density measurements of Montreal for battery-free IoT sensor network planning," *IEEE Internet Things J.*, vol. 8, no. 17, pp. 13209–13221, Sep. 2021, doi: 10.1109/JIOT.2021.3065683.

[37] J. Tavares, N. Barroca, H. M. Saraiva, L. M. Borges, F. J. Velez, C. Loss, R. Salvado, P. Pinho, R. Gonçalves, and N. B. Carvalho, "Spectrum opportunities for electromagnetic energy harvesting from 350 MHz to 3 GHz," in *Proc. 7th Int. Symp. Med. Inf. Commun. Technol. (ISMICT)*, Mar. 2013, pp. 126–130, doi: 10.1109/ISMICT.2013.6521714.

[38] M. Pinuela, P. D. Mitcheson, and S. Lucyszyn, "Ambient RF energy harvesting in urban and semi-urban environments," *IEEE Trans. Microw. Theory Techn.*, vol. 61, no. 7, pp. 2715–2726, Jul. 2013, doi: 10.1109/TMTT.2013.2262687.

[39] Y. Lu, H. Dai, M. Huang, M.-K. Law, S.-W. Sin, U. Seng-Pan, and R. P. Martins, "A wide input range dual-path CMOS rectifier for RF energy harvesting," *IEEE Trans. Circuits Syst. II, Exp. Briefs*, vol. 64, no. 2, pp. 166–170, Apr. 2017, doi: 10.1109/TCSII.2016.2554778.
[40] M. Arrawatia, M. S. Baghini, and G. Kumar, "Differential microstrip antenna for RF energy harvesting," *IEEE Trans. Antennas Propag.*, vol. 63, no. 4, pp. 1581–1588, Apr. 2015, doi: 10.1109/TAP.2015.2399939.
[41] C. A. Balanis, *Antenna Theory: Analysis and Design*. Hoboken, NJ, USA: Wiley, 2015.
[42] H.-N. Dai, K.-W. Ng, M. Li, and M.-Y. Wu, "An overview of using directional antennas in wireless networks," *Int. J. Commun. Syst.*, vol. 26, no. 4, pp. 413–448, 2013.
[43] A. T. Mobashsher and A. M. Abbosh, "Performance of directional and omnidirectional antennas in wideband head imaging," *IEEE Antennas Wireless Propag. Lett.*, vol. 15, pp. 1618–1621, 2016, doi: 10.1109/LAWP.2016.2519527.
[44] E. Muehldorf, M. Teichman, and E. Kramer, "Polarization mismatch errors in radio phase interferometers," *IEEE Trans. Aerosp. Electron. Syst.*, vol. AES-8, no. 2, pp. 135–141, Mar. 1972, doi: 10.1109/TAES.1972.309481.
[45] H. L. Thal Jr., "Radiation efficiency limits for elementary antenna shapes," *IEEE Trans. Antennas Propag.*, vol. 66, no. 5, pp. 2179–2187, May 2018, doi: 10.1109/TAP.2018.2809507.
[46] A. Gangwar and M. S. Alam, "A high FoM monopole antenna with asymmetrical L-slots for WiMAX and WLAN applications," *Microw. Opt. Technol. Lett.*, vol. 60, no. 1, pp. 196–202, Jan. 2018, doi: 10.1002/mop.30941.
[47] M. A. Ullah, R. Keshavarz, M. Abolhasan, J. Lipman, K. P. Esselle, and N. Shariati, "A review on antenna technologies for ambient RF energy harvesting and wireless power transfer: Designs, challenges and applications," *IEEE Access*, vol. 10, pp. 17231–17267, 2022, doi: 10.1109/ACCESS.2022.3149276.
[48] M. Alibakhshikenari, M. Naser-Moghadasi, R. Sadeghzadeh, B. S. Virdee, and E. Limiti, "Printed planar antenna designs based on metamaterial unit-cells for broadband wireless communication systems," in *Microstrip Antennas: Trends in Research*. London, U.K.: IntechOpen, 2017.
[49] A. Georgiadis, G. V. Andia, and A. Collado, "Rectenna design and optimization using reciprocity theory and harmonic balance analysis for electromagnetic (EM) energy harvesting," *IEEE Antennas Wireless Propag. Lett.*, vol. 9, pp. 444–446, 2010, doi: 10.1109/LAWP.2010.2050131.
[50] S. Ghosh, "Design and testing of RF energy harvesting module in GSM 900 band using circularly polarized antenna," in *Proc. IEEE Int. Conf. Res. Comput. Intell. Commun. Netw. (ICRCICN)*, Nov. 2015, pp. 386–389, doi: 10.1109/ICRCICN.2015.7434269.
[51] L. B. K. Bernard and A. Alphones, "AN e-shaped slotted-circular-patch antenna for circularly polarized radiation and radiofrequency energy harvesting," *Microw. Opt. Technol. Lett.*, vol. 58, no. 4, pp. 868–875, Apr. 2016, doi: 10.1002/mop.29689.
[52] U. Olgun, C.-C. Chen, and J. L. Volakis, "Design of an efficient ambient WiFi energy harvesting system," *IET Microw., Antennas Propag.*, vol. 6, no. 11, pp. 1200–1206, Aug. 2012, doi: 10.1049/iet-map.2012.0129.
[53] Y. Y. Shi, J. Jing, Y. Fan, L. Yang, and M. Wang, "Design of a novel compact and efficient rectenna for WiFi energy harvesting," *Prog. Electromagn. Res.*, vol. 83, pp. 57–70, 2018, doi: 10.2528/PIERC18012803.
[54] G. Monti, F. Congedo, D. De Donno, and L. Tarricone, "Monopole-based rectenna for microwave energy harvesting of UHF RFID systems," *Prog. Electromagn. Res. C*, vol. 31, pp. 109–121, 2012.
[55] S. Ladan, N. Ghassemi, A. Ghiotto, and K. Wu, "Highly efficient compact rectenna for wireless energy harvesting application," *IEEE Microw. Mag.*, vol. 14, no. 1, pp. 117–122, Jan. 2013, doi: 10.1109/MMM.2012.2226629.
[56] T.-L. Nguyen, Y. Sato, and K. Ishibashi, "7.6 μW ambient energy harvesting rectenna from LTE mobile phone signal for IoT applications," in *Proc. Int. Conf. Adv. Technol. Commun. (ATC)*, Oct. 2020, pp. 45–49, doi: 10.1109/ATC50776.2020.9255471.
[57] R.-H. Chen, Y.-C. Lee, and J.-S. Sun, "Design and experiment of a rectifying antenna for 900 MHz wireless power transmission," in *Proc. Asia–Pacific Microw. Conf.*, Dec. 2008, pp. 1–4, doi: 10.1109/APMC.2008.4958600.
[58] K. R. Sadagopan, J. Kang, Y. Ramadass, and A. Natarajan, "A cm-scale 2.4-GHz wireless energy harvester with nanowatt boost converter and antenna-rectifier resonance for WiFi powering of sensor nodes," *IEEE J. Solid-State Circuits*, vol. 53, no. 12, pp. 3396–3406, Dec. 2018, doi: 10.1109/JSSC.2018.2875465.
[59] J. Kang, P. Y. Chiang, and A. Natarajan, "A 1.2 cm^2 2.4 GHz self-oscillating rectifier-antenna achieving −34.5 dBm sensitivity for wirelessly powered sensors," in *IEEE Int. Solid-State Circuits Conf. (ISSCC) Dig. Tech. Papers*, Jan. 2016, pp. 374–375, doi: 10.1109/ISSCC.2016.7418063.
[60] S. Bhunia, "Effects of slot loading on microstrip patch antennas," *Int. J. Wired Wireless Commun.*, vol. 1, no. 1, pp. 1–6, 2012.
[61] Y. Shi, J. Jing, Y. Fan, L. Yang, Y. Li, and M. Wang, "A novel compact broadband rectenna for ambient RF energy harvesting," *AEU-Int. J. Electron. Commun.*, vol. 95, pp. 264–270, Oct. 2018, doi: 10.1016/j.aeue.2018.08.035.
[62] D. M. Pozar, *Microwave Engineering*, 4th ed. Hoboken, NJ, USA: Wiley, 2012.
[63] C.-H. Li, M.-C. Yu, and H.-J. Lin, "A compact 0.9-/2.6-GHz dual-band RF energy harvester using SiP technique," *IEEE Microw. Wireless Compon. Lett.*, vol. 27, no. 7, pp. 666–668, Jun. 2017, doi: 10.1109/LMWC.2017.2711506.
[64] M. Thompson and J. K. Fidler, "Determination of the impedance matching domain of impedance matching networks," *IEEE Trans. Circuits Syst. I, Reg. Papers*, vol. 51, no. 10, pp. 2098–2106, Oct. 2004, doi: 10.1109/TCSI.2004.835682.
[65] M. A. Karami and K. Moez, "Systematic co-design of matching networks and rectifiers for CMOS radio frequency energy harvesters," *IEEE Trans. Circuits Syst. I, Reg. Papers*, vol. 66, no. 8, pp. 3238–3251, Aug. 2019, doi: 10.1109/TCSI.2019.2902506.
[66] D. Lauder and Y. Sun, "Design considerations of antennas and adaptive impedance matching networks for RF energy harvesting," in *Proc. Eur. Conf. Circuit Theory Design (ECCTD)*, Sep. 2020, pp. 1–4, doi: 10.1109/ECCTD49232.2020.9218310.
[67] Y. Han and D. J. Perreault, "Analysis and design of high efficiency matching networks," *IEEE Trans. Power Electron.*, vol. 21, no. 5, pp. 1484–1491, Sep. 2006, doi: 10.1109/TPEL.2006.882083.
[68] G. C. Martins and W. A. Serdijn, "Multistage complex-impedance matching network analysis and optimization," *IEEE Trans. Circuits Syst. II, Exp. Briefs*, vol. 63, no. 9, pp. 833–837, Sep. 2016, doi: 10.1109/TCSII.2016.2534738.
[69] P.-H. Hsieh, C.-H. Chou, and T. Chiang, "An RF energy harvester with 44.1% PCE at input available power of −12 dBm," *IEEE Trans. Circuits Syst. I, Reg. Papers*, vol. 62, no. 6, pp. 1528–1537, Jun. 2015, doi: 10.1109/TCSI.2015.2418834.
[70] Y. Wang and M. Sawan, "High-efficiency CMOS rectifier dedicated for multi-band ambient RF energy harvesting," in *Proc. 21st IEEE Int. Conf. Electron., Circuits Syst. (ICECS)*, Dec. 2014, pp. 179–182, doi: 10.1109/ICECS.2014.7049951.
[71] N. Eltresy, D. Eisheakh, E. Abdallah, and H. Elhenawy, "RF energy harvesting using efficiency dual band rectifier," in *Proc. Asia–Pacific Microw. Conf. (APMC)*, Nov. 2018, pp. 1453–1455, doi: 10.23919/APMC.2018.8617347.
[72] T. Hirakawa and N. Shinohara, "Theoretical analysis of single shunt rectifiers," in *Proc. IEEE Wireless Power Transf. Conf. (WPTC)*, Jun. 2019, pp. 578–581, doi: 10.1109/WPTC45513.2019.9055534.
[73] A. Mouapi and N. Hakem, "A selective rectifier for RF energy harvesting for IoT applications," in *Proc. IEEE Int. Symp. Antennas Propag. USNC/URSI Nat. Radio Sci. Meeting*, Jul. 2018, pp. 2523–2524, doi: 10.1109/APUSNCURSINRSM.2018.8608705.
[74] S. Park, J. Yang, and J. Rivas-Davila, "A hybrid Cockcroft–Walton/Dickson multiplier for high voltage generation," *IEEE Trans. Power Electron.*, vol. 35, no. 3, pp. 2714–2723, Mar. 2020, doi: 10.1109/TPEL.2019.2929167.
[75] M. Awad, P. Benech, and J.-M. Duchamp, "Design of Dickson rectifier for RF energy harvesting in 28 nm FD-SOI technology," in *Proc. Joint Int. EUROSOI Workshop Int. Conf. Ultimate Integr. Silicon (EUROSOI-ULIS)*, Mar. 2018, pp. 1–4, doi: 10.1109/ULIS.2018.8354751.
[76] U. Guler, Y. Jia, and M. Ghovanloo, "A reconfigurable passive RF-to-DC converter for wireless IoT applications," *IEEE Trans. Circuits Syst. II, Exp. Briefs*, vol. 66, no. 11, pp. 1800–1804, Nov. 2019, doi: 10.1109/TCSII.2019.2894562.

[77] L. Ramalingam, S. Mariappan, P. Parameswaran, J. Rajendran, R. S. Nitesh, N. Kumar, A. Nathan, and B. S. Yarman, "The advancement of radio frequency energy harvesters (RFEHs) as a revolutionary approach for solving energy crisis in wireless communication devices: A review," *IEEE Access*, vol. 9, pp. 106107–106139, 2021, doi: 10.1109/ACCESS.2021.3098895.

[78] P. Li, Z. Long, and Z. Yang, "RF energy harvesting for batteryless and maintenance-free condition monitoring of railway tracks," *IEEE Internet Things J.*, vol. 8, no. 5, pp. 3512–3523, Mar. 2021, doi: 10.1109/JIOT.2020.3023475.

[79] K. Kotani and T. Ito, "High efficiency CMOS rectifier circuit with self-Vth-cancellation and power regulation functions for UHF RFIDs," in *Proc. IEEE Asian Solid-State Circuits Conf.*, Nov. 2007, pp. 119–122, doi: 10.1109/ASSCC.2007.4425746.

[80] K. Kotani and T. Ito, "Self-Vth-cancellation high-efficiency CMOS rectifier circuit for UHF RFIDs," *IEICE Trans. Electron.*, vol. E92-C, no. 1, pp. 153–160, 2009, doi: 10.1587/transele.E92.C.153.

[81] G. Papotto, F. Carrara, and G. Palmisano, "A 90-nm CMOS threshold-compensated RF energy harvester," *IEEE J. Solid-State Circuits*, vol. 46, no. 9, pp. 1985–1997, Sep. 2011, doi: 10.1109/JSSC.2011.2157010.

[82] L. Xia, J. Cheng, N. E. Glover, and P. Chiang, "0.56 V, −20 dBm RF-powered, multi-node wireless body area network system-on-a-chip with harvesting-efficiency tracking loop," *IEEE J. Solid-State Circuits*, vol. 49, no. 6, pp. 1345–1355, Jun. 2014, doi: 10.1109/JSSC.2014.2305074.

[83] H. Nakamoto, D. Yamazaki, T. Yamamoto, H. Kurata, S. Yamada, K. Mukaida, T. Ninomiya, T. Ohkawa, S. Masui, and K. Gotoh, "A passive UHF RF identification CMOS tag IC using ferroelectric RAM in 0.35-μm technology," *IEEE J. Solid-State Circuits*, vol. 42, no. 1, pp. 101–110, Dec. 2007, doi: 10.1109/JSSC.2006.886523.

[84] H. Nakamoto, D. Yamazaki, T. Yamamoto, H. Kurata, S. Yamada, K. Mukaida, T. Ninomiya, T. Ohkawa, S. Masui, and K. Gotoh, "A passive UHF RFID tag LSI with 36.6% efficiency CMOS-only rectifier and current-mode demodulator in 0.35 μm FeRAM technology," in *IEEE Int. Solid-State Circuits Conf. (ISSCC) Dig. Tech. Papers*, Feb. 2006, pp. 1201–1210, doi: 10.1109/ISSCC.2006.1696166.

[85] T. Le, K. Mayaram, and T. Fiez, "Efficient far-field radio frequency energy harvesting for passively powered sensor networks," *IEEE J. Solid-State Circuits*, vol. 43, no. 5, pp. 1287–1302, May 2008, doi: 10.1109/JSSC.2008.920318.

[86] H. Dai, Y. Lu, M.-K. Law, S.-W. Sin, U. Seng-Pan, and R. P. Martins, "A review and design of the on-chip rectifiers for RF energy harvesting," in *Proc. IEEE Int. Wireless Symp.*, Mar. 2015, pp. 1–4, doi: 10.1109/IEEE-IWS.2015.7164642.

[87] R. Barnett, G. Balachandran, S. Lazar, B. Kramer, G. Konnail, S. Rajasekhar, and V. Drobny, "A passive UHF RFID transponder for EPC Gen 2 with −14 dBm sensitivity in 0.13 μm CMOS," in *IEEE Int. Solid-State Circuits Conf. (ISSCC) Dig. Tech. Papers*, Feb. 2007, pp. 582–623, doi: 10.1109/ISSCC.2007.373554.

[88] Z. Hameed and K. Moez, "Hybrid forward and backward threshold-compensated RF–DC power converter for RF energy harvesting," *IEEE J. Emerg. Sel. Topics Circuits Syst.*, vol. 4, no. 3, pp. 335–343, Sep. 2014, doi: 10.1109/JETCAS.2014.2337211.

[89] Y.-S. Luo and S.-L. Liu, "A voltage multiplier with adaptive threshold voltage compensation," *IEEE J. Solid-State Circuits*, vol. 52, no. 8, pp. 2208–2214, Aug. 2017, doi: 10.1109/JSSC.2017.2693228.

[90] T. Umeda, H. Yoshida, S. Sekine, Y. Fujita, T. Suzuki, and S. Otaka, "A 950-MHz rectifier circuit for sensor network tags with 10-m distance," *IEEE J. Solid-State Circuits*, vol. 41, no. 1, pp. 35–41, Jan. 2006, doi: 10.1109/JSSC.2005.858620.

[91] H. Reinisch, M. Wiessflecker, S. Gruber, H. Unterassinger, G. Hofer, M. Klamminger, W. Pribyl, and G. Holweg, "A multifrequency passive sensing tag with on-chip temperature sensor and off-chip sensor interface using EPC HF and UHF RFID technology," *IEEE J. Solid-State Circuits*, vol. 46, no. 12, pp. 3075–3088, Oct. 2011, doi: 10.1109/JSSC.2011.2167548.

[92] M. H. Ouda, W. Khalil, and K. N. Salama, "Wide-range adaptive RF-to-DC power converter for UHF RFIDs," *IEEE Microw. Wireless Compon. Lett.*, vol. 26, no. 8, pp. 634–636, Aug. 2016, doi: 10.1109/LMWC.2016.2586077.

[93] H. Kim and I. Kwon, "Design of high-efficiency CMOS rectifier with low reverse leakage for RF energy harvesting," *Electron. Lett.*, vol. 55, no. 8, pp. 446–448, Apr. 2019, doi: 10.1049/el.2018.8143.

[94] S. S. Hashemi, M. Sawan, and Y. Savaria, "A high-efficiency low-voltage CMOS rectifier for harvesting energy in implantable devices," *IEEE Trans. Biomed. Circuits Syst.*, vol. 6, no. 4, pp. 326–335, Aug. 2012, doi: 10.1109/TBCAS.2011.2177267.

[95] S. R. Khan and G. S. Choi, "High-efficiency CMOS rectifier with minimized leakage and threshold cancellation features for low power bio-implants," *Microelectron. J.*, vol. 66, pp. 67–75, Aug. 2017, doi: 10.1016/j.mejo.2017.06.002.

[96] C. Song, Y. Huang, P. Carter, J. Zhou, S. Yuan, Q. Xu, and M. Kod, "A novel six-band dual CP rectenna using improved impedance matching technique for ambient RF energy harvesting," *IEEE Trans. Antennas Propag.*, vol. 64, no. 7, pp. 3160–3171, May 2016, doi: 10.1109/TAP.2016.2565697.

[97] V. Kuhn, C. Lahuec, F. Seguin, and C. Person, "A multi-band stacked RF energy harvester with RF-to-DC efficiency up to 84%," *IEEE Trans. Microw. Theory Techn.*, vol. 63, no. 5, pp. 1768–1778, May 2015, doi: 10.1109/TMTT.2015.2416233.

[98] O. Kazanc, F. Maloberti, and C. Dehollain, "High-Q adaptive matching network for remote powering of UHF RFIDs and wireless sensor systems," in *Proc. IEEE Topical Conf. Wireless Sensors Sensor Netw. (WiSNet)*, Jan. 2013, pp. 10–12, doi: 10.1109/WiSNet.2013.6488617.

[99] P. Xu, D. Flandre, and D. Bol, "Analysis and design of RF energy-harvesting systems with impedance-aware rectifier sizing," *IEEE Trans. Circuits Syst. II, Exp. Briefs*, vol. 70, no. 2, pp. 361–365, Feb. 2023, doi: 10.1109/TCSII.2022.3171470.

[100] W. X. Lian, H. Ramiah, and G. Chong, "A differential RF front-end CMOS transformer matching for ambient RF energy harvesting systems," in *Proc. IEEE Asia Pacific Conf. Circuit Syst. (APCCAS)*, Nov. 2021, pp. 133–136, doi: 10.1109/APCCAS51387.2021.9687725.

[101] L. M. Borges, N. Barroca, H. M. Saraiva, J. Tavares, P. T. Gouveia, F. J. Velez, C. Loss, R. Salvado, P. Pinho, R. Goncalves, N. B. Carvalho, R. Chavez-Santiago, and I. Balasingham, "Design and evaluation of multi-band RF energy harvesting circuits and antennas for WSNs," in *Proc. 21st Int. Conf. Telecommun. (ICT)*, May 2014, pp. 308–312, doi: 10.1109/ICT.2014.6845129.

[102] D.-K. Ho, I. Kharrat, V.-D. Ngo, T.-P. Vuong, Q.-C. Nguyen, and M.-T. Le, "Dual-band rectenna for ambient RF energy harvesting at GSM 900 MHz and 1800 MHz," in *Proc. IEEE Int. Conf. Sustain. Energy Technol. (ICSET)*, Nov. 2016, pp. 306–310, doi: 10.1109/ICSET.2016.7811800.

[103] S. Muhammad, J. J. Tiang, S. K. Wong, A. Smida, R. Ghayoula, and A. Iqbal, "A dual-band ambient energy harvesting rectenna design for wireless power communications," *IEEE Access*, vol. 9, pp. 99944–99953, 2021, doi: 10.1109/ACCESS.2021.3096834.

[104] Z. Liang and J. Yuan, "A compact dual-band four-port ambient RF energy harvester with high-sensitivity, high-efficiency, and wide power range," *IEEE Trans. Microw. Theory Techn.*, vol. 70, no. 1, pp. 641–649, Jan. 2022, doi: 10.1109/TMTT.2021.3106310.

[105] K. Niotaki, S. Kim, S. Jeong, A. Collado, A. Georgiadis, and M. M. Tentzeris, "A compact dual-band rectenna using slot-loaded dual band folded dipole antenna," *IEEE Antennas Wireless Propag. Lett.*, vol. 12, pp. 1634–1637, 2013, doi: 10.1109/LAWP.2013.2294200.

[106] S. Chandravanshi, S. S. Sarma, and M. J. Akhtar, "Design of triple band differential rectenna for RF energy harvesting," *IEEE Trans. Antennas Propag.*, vol. 66, no. 6, pp. 2716–2726, Jun. 2018, doi: 10.1109/TAP.2018.2819699.

[107] S. Roy, J. J. Tiang, M. B. Roslee, M. T. Ahmed, A. Z. Kouzani, and M. A. P. Mahmud, "Quad-band rectenna for ambient radio frequency (RF) energy harvesting," *Sensors*, vol. 21, no. 23, p. 7838, Nov. 2021, doi: 10.3390/s21237838.

[108] S. Roy, R. J.-J. Tiang, M. B. Roslee, M. T. Ahmed, and M. A. P. Mahmud, "Quad-band multiport rectenna for RF energy harvesting in ambient environment," *IEEE Access*, vol. 9, pp. 77464–77481, 2021, doi: 10.1109/ACCESS.2021.3082914.

[109] S. Shen, C.-Y. Chiu, and R. D. Murch, "A dual-port triple-band L-probe microstrip patch rectenna for ambient RF energy harvesting," *IEEE Antennas Wireless Propag. Lett.*, vol. 16, pp. 3071–3074, 2017, doi: 10.1109/LAWP.2017.2761397.

[110] H. Sun, Y.-X. Guo, M. He, and Z. Zhong, "A dual-band rectenna using broadband Yagi antenna array for ambient RF power harvesting," *IEEE Antennas Wireless Propag. Lett.*, vol. 12, pp. 918–921, 2013, doi: 10.1109/LAWP.2013.2272873.

[111] C. Song, Y. Huang, J. Zhou, J. Zhang, S. Yuan, and P. Carter, "A high-efficiency broadband rectenna for ambient wireless energy harvesting," *IEEE Trans. Antennas Propag.*, vol. 63, no. 8, pp. 3486–3495, Aug. 2015, doi: 10.1109/TAP.2015.2431719.

[112] M. Arrawatia, M. S. Baghini, and G. Kumar, "Broadband bent triangular omnidirectional antenna for RF energy harvesting," *IEEE Antennas Wireless Propag. Lett.*, vol. 15, pp. 36–39, 2016, doi: 10.1109/LAWP.2015.2427232.

[113] C. Song, Yi Huang, J. Zhou, P. Carter, S. Yuan, Q. Xu, and Z. Fei, "Matching network elimination in broadband rectennas for high-efficiency wireless power transfer and energy harvesting," *IEEE Trans. Ind. Electron.*, vol. 64, no. 5, pp. 3950–3961, Dec. 2017, doi: 10.1109/TIE.2016.2645505.

[114] M. Wagih, G. S. Hilton, A. S. Weddell, and S. Beeby, "Dual-band dual-mode textile antenna/rectenna for simultaneous wireless information and power transfer (SWIPT)," *IEEE Trans. Antennas Propag.*, vol. 69, no. 10, pp. 6322–6332, Oct. 2021, doi: 10.1109/TAP.2021.3070230.

[115] J. Liu, Y. Z. Xiu, and C. L. Yang, "Analysis and design of dual-band rectifier using novel matching network," *IEEE Trans. Circuits Syst. II, Exp. Briefs*, vol. 65, no. 4, pp. 431–435, Apr. 2017, doi: 10.1109/TCSII.2017.2698464.

[116] S. Li, F. Cheng, C. Gu, S. Yu, and K. Huang, "Efficient dual-band rectifier using stepped impedance stub matching network for wireless energy harvesting," *IEEE Microw. Wireless Compon. Lett.*, vol. 31, no. 7, pp. 921–924, Jul. 2021, doi: 10.1109/LMWC.2021.3078546.

[117] J. Liu, M. Huang, and Z. Du, "Design of compact dual-band RF rectifiers for wireless power transfer and energy harvesting," *IEEE Access*, vol. 8, pp. 184901–184908, 2020, doi: 10.1109/ACCESS.2020.3029603.

[118] M. Huang, Y. L. Lin, J.-H. Ou, X. Y. Zhang, Q. W. Lin, W. Che, and Q. Xue, "Single- and dual-band RF rectifiers with extended input power range using automatic impedance transforming," *IEEE Trans. Microw. Theory Techn.*, vol. 67, no. 5, pp. 1974–1984, May 2019, doi: 10.1109/TMTT.2019.2901443.

[119] H. Tafekirt, J. Pelegri-Sebastia, A. Bouajaj, and B. M. Reda, "A sensitive triple-band rectifier for energy harvesting applications," *IEEE Access*, vol. 8, pp. 73659–73664, 2020, doi: 10.1109/ACCESS.2020.2986797.

[120] J.-J. Lu, X.-X. Yang, H. Mei, and C. Tan, "A four-band rectifier with adaptive power for electromagnetic energy harvesting," *IEEE Microw. Wireless Compon. Lett.*, vol. 26, no. 10, pp. 819–821, Oct. 2017, doi: 10.1109/LMWC.2016.2601294.

[121] Z. Liu, Z. Zhong, and Y.-X. Guo, "Enhanced dual-band ambient RF energy harvesting with ultra-wide power range," *IEEE Microw. Wireless Compon. Lett.*, vol. 25, no. 9, pp. 630–632, Sep. 2015, doi: 10.1109/LMWC.2015.2451397.

[122] K. Niotaki, A. Georgiadis, A. Collado, and J. S. Vardakas, "Dual-band resistance compression networks for improved rectifier performance," *IEEE Trans. Microw. Theory Techn.*, vol. 62, no. 12, pp. 3512–3521, Dec. 2014, doi: 10.1109/TMTT.2014.2364830.

[123] M. U. Rehman, W. Ahmad, and W. T. Khan, "Highly efficient dual band 2.45/5.85 GHz rectifier for RF energy harvesting applications in ISM band," in *Proc. IEEE Asia Pacific Microw. Conf. (APMC)*, Nov. 2017, pp. 150–153, doi: 10.1109/APMC.2017.8251400.

[124] G.-M. Sung, H.-Y. Chou, and Z.-W. Chen, "Radio frequency energy harvesting IC for ISM-915 MHz and 2.45 GHz wireless transmitter," in *Proc. IEEE Int. Future Energy Electron. Conf. (IFEEC)*, Nov. 2021, pp. 1–5, doi: 10.1109/IFEEC53238.2021.9661737.

[125] J. S. Gaggatur and S. F. S. Vajrala, "An 860 MHz–1960 MHz multi-band multi-stage rectifier for RF energy harvesting in 130 nm CMOS," in *Proc. IEEE Int. Conf. Electron., Comput. Commun. Technol. (CONECCT)*, Jul. 2020, pp. 1–4, doi: 10.1109/CONECCT50063.2020.9198677.

[126] D. Lee, T. Kim, S. Kim, K. Byun, and K. Kwon, "A CMOS rectifier with 72.3% RF-to-DC conversion efficiency employing tunable impedance matching network for ambient RF energy harvesting," in *Proc. Int. SoC Design Conf. (ISOCC)*, Nov. 2018, pp. 259–260, doi: 10.1109/ISOCC.2018.8649983.

[127] A. Leoni, L. Pantoli, V. Stornelli, G. Ferri, M. Russo, and P. Solic, "90/900 MHz IC architecture for autonomous systems," in *Proc. 2nd Int. Multidisciplinary Conf. Comput. Energy Sci. (SpliTech)*, Jul. 2017, pp. 1–4.

[128] H. D. Hernandez, D. A. Pontes, B. Soares, D. de Carvalho, and W. Van Noije, "Dual-band GSM energy harvester for a duty-cycle approach in 180 nm CMOS technology," in *Proc. IEEE 34th Int. System-Chip Conf. (SOCC)*, Sep. 2021, pp. 29–33, doi: 10.1109/SOCC52499.2021.9739239.

[129] B.-R. Heo and I. Kwon, "A dual-band wide-input-range adaptive CMOS RF–DC converter for ambient RF energy harvesting," *Sensors*, vol. 21, no. 22, p. 7483, Nov. 2021, doi: 10.3390/s21227483.

[130] D. Khan, K.-Y. Lee, S. J. Oh, K. Shehzad, D. Verma, Z. H. N. Khan, Y. G. Pu, M. Lee, K. C. Hwang, and Y. Yang, "A CMOS RF energy harvester with 47% peak efficiency using internal threshold voltage compensation," *IEEE Microw. Wireless Compon. Lett.*, vol. 29, no. 6, pp. 415–417, Jun. 2019, doi: 10.1109/LMWC.2019.2909403.

[131] S. M. Noghabaei, R. L. Radin, and M. Sawan, "Efficient dual-band ultra-low-power RF energy harvesting front-end for wearable devices," in *Proc. IEEE 61st Int. Midwest Symp. Circuits Syst. (MWSCAS)*, Aug. 2018, pp. 444–447, doi: 10.1109/MWSCAS.2018.8623832.

[132] I. Ulisse, L. Pantoli, and G. Ferri, "A multiband 150 nm CMOS energy harvester architecture," in *Proc. PhotonIcs Electromagn. Res. Symp.-Spring*, Jun. 2019, pp. 1165–1170, doi: 10.1109/PIERS-Spring46901.2019.9017235.

[133] Z. Zeng, S. Shen, B. Wang, J. J. Estrada-Lopez, R. Murch, and E. Sanchez-Sinencio, "An ultra-low-power power management circuit with output bootstrapping and reverse leakage reduction function for RF energy harvesting," in *IEEE MTT-S Int. Microw. Symp. Dig.*, Aug. 2020, pp. 1059–1062, doi: 10.1109/IMS30576.2020.9224098.

[134] Y. Tian, L. Liu, and J. Ma, "A high-sensitivity, low-noise dual-band RF energy harvesting and managing system for wireless bio-potential acquisition," *Microelectron. J.*, vol. 116, Oct. 2021, Art. no. 105239, doi: 10.1016/j.mejo.2021.105239.

[135] W. X. Lian, H. Ramiah, G. Chong, K. K. P. Churchill, N. S. Lai, Y. Chen, P.-I. Mak, and R. P. Martins, "A −20-dBm sensitivity RF energy-harvesting rectifier front end using a transformer IMN," *IEEE Trans. Very Large Scale Integr. (VLSI) Syst.*, vol. 30, no. 11, pp. 1808–1812, Nov. 2022, doi: 10.1109/TVLSI.2022.3207158.

[136] A. N. Parks and J. R. Smith, "Active power summation for efficient multiband RF energy harvesting," in *IEEE MTT-S Int. Microw. Symp. Dig.*, May 2015, pp. 1–4, doi: 10.1109/MWSYM.2015.7167129.

[137] A. N. Parks and J. R. Smith, "Sifting through the airwaves: Efficient and scalable multiband RF harvesting," in *Proc. IEEE Int. Conf. RFID (IEEE RFID)*, Apr. 2014, pp. 74–81, doi: 10.1109/RFID.2014.6810715.

[138] M. Taghadosi, L. Albasha, N. A. Quadir, Y. A. Rahama, and N. Qaddoumi, "High efficiency energy harvesters in 65 nm CMOS process for autonomous IoT sensor applications," *IEEE Access*, vol. 6, pp. 2397–2409, 2018, doi: 10.1109/ACCESS.2017.2783045.

[139] G. Chong, H. Ramiah, J. Yin, J. Rajendran, P.-I. Mak, and R. P. Martins, "A wide-PCE-dynamic-range CMOS cross-coupled differential-drive rectifier for ambient RF energy harvesting," *IEEE Trans. Circuits Syst. II, Exp. Briefs*, vol. 68, no. 6, pp. 1743–1747, Jun. 2021, doi: 10.1109/TCSII.2019.2937542.

[140] B. Li, X. Shao, N. Shahshahan, N. Goldsman, T. Salter, and G. M. Metze, "An antenna co-design dual band RF energy harvester," *IEEE Trans. Circuits Syst. I, Reg. Papers*, vol. 60, no. 12, pp. 3256–3266, Dec. 2013, doi: 10.1109/TCSI.2013.2264712.

[141] C. S. Shailesh and H. Kari, "A novel cascading scheme to improve the performance of voltage multiplier circuits," *Analog Integr. Circuits Signal Process.*, vol. 84, no. 3, pp. 373–381, 2015, doi: 10.1007/s10470-015-0595-y.

[142] J. A. Hagerty, F. B. Helmbrecht, W. H. McCalpin, R. Zane, and Z. B. Popovic, "Recycling ambient microwave energy with broad-band rectenna arrays," *IEEE Trans. Microw. Theory Techn.*, vol. 52, no. 3, pp. 1014–1024, Mar. 2004, doi: 10.1109/TMTT.2004.823585.

YI CHEN LEE was born in Kuala Lumpur, Malaysia. He received the B.E. degree (Hons.) in mechatronic engineering from the Asia Pacific University of Technology and Innovation, Kuala Lumpur, in 2022. He is currently pursuing the M.Sc. degree with the Department of Electrical Engineering, University of Malaya, Kuala Lumpur. His main research interests include micro-energy harvesting, power management ICs, and analog integrated circuits design.

HARIKRISHNAN RAMIAH (Senior Member, IEEE) received the B.Eng. (Hons.), M.Sc., and Ph.D. degrees in electrical and electronic engineering (analog and digital IC design) from Universiti Sains Malaysia, Penang, Malaysia, in 2000, 2003, and 2008, respectively.

In 2002, he was with Intel Technology Sdn. Bhd., Penang, where he performed high-frequency signal integrity analysis. In 2003, he was with Sires Labs Sdn. Bhd., Cyberjaya. He is currently a Professor with the Department of Electrical Engineering, University of Malaya, Kuala Lumpur, Malaysia, working in the area of RF integrated circuit (RFIC) and RF energy harvesting circuit design. He is also the Director of the Center of Research Industry 4.0 (CRI 4.0), University of Malaya. He has authored or coauthored several articles in technical publications. His main research interests include analog-integrated circuit design, RFIC design, VLSI system design, and radio frequency energy harvesting power management module design.

Prof. Ramiah is a member of the Institute of Electronics, Information, and Communication Engineers. He was a recipient of the Intel Fellowship Grant Award, from 2000 to 2008. He has received a continuous international research funding in recognition of his work, from 2014 to 2021, such as the Motorola Foundation Grant. He is a Chartered Engineer of the Institute of Electrical Technology and a Professional Engineer registered under the Board of Engineers Malaysia.

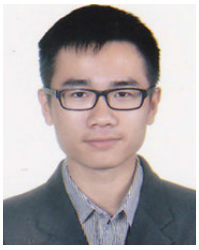

ALEXANDER CHOO (Graduated Student Member, IEEE) was born in Penang, Malaysia. He received the B.Eng. degree (Hons.) in electrical engineering from the University of Malaya, Kuala Lumpur, Malaysia, in 2018, where he is currently pursuing the Ph.D. degree with the Department of Electrical Engineering. His research interests include energy harvesting front ends, power management ICs, and analog/RF integrated circuit design.

KISHORE KUMAR PAKKIRISAMI CHURCHILL (Graduate Student Member, IEEE) was born in Thanjavur, India. He received the B.E. degree in electronics and communication engineering and the M.E. degree in VLSI design from Anna University, Chennai, in 2010 and 2012, respectively. He is currently pursuing the Ph.D. degree with the Department of Electrical Engineering, University of Malaya, Kuala Lumpur, Malaysia. His research interests include micro energy harvesting, analog/RF integrated circuit design, VLSI system design, power management ICs, and WSN.

NAI SHYAN LAI received the B.Eng. degree (Hons.) in electrical engineering and the Ph.D. degree in silicon-based nanoelectronics and radiation detectors from the University of New South Wales, in 2007 and 2012, respectively. He is currently an Associate Professor with the School of Engineering, Asia Pacific University of Technology and Innovation, working in the area of micro- and nano-electronics. Since 2009, he has been publishing most of his research work in the IEEE Transactions, the American Institute of Physics, the American Physical Society, and Nature Group journals. His research interests include semiconductor micro- and nano-fabrication, quantum dot devices, cryogenic temperature measurements, single electron transistors, quantum computation, and silicon microdosimeters.

CHEE CHEOW LIM was born in Kuala Lumpur, Malaysia. He received the B.Eng. degree (Hons.) in electrical and electronic engineering from the Asia Pacific University of Technology and Innovation (APU), Malaysia, in 2014, and the Ph.D. degree in electrical engineering from the University of Malaya (UM), Kuala Lumpur, in 2019. From 2021 to 2022, he was an Analog Engineer at Intel Corporation. He is currently a Lecturer with APU. His research interests include CMOS RF integrated circuits and systems with specialization in RF oscillators, and modeling and characterization of passive inductors/transformers. He received the Best Undergraduate Final Year Project Award, in 2014; the IEEE ISSCC 2018 Student Travel Grant Award; and the IEEE SSCS Predoctoral Achievement Award, in 2018 and 2019.

YONG CHEN (Senior Member, IEEE) received the B.Eng. degree in electronic and information engineering from the Communication University of China (CUC), Beijing, China, in 2005, and the Ph.D. (Eng.) degree in microelectronics and solid-state electronics from the Institute of Microelectronics, Chinese Academy of Sciences (IMECAS), Beijing, in 2010. From 2010 to 2013, he worked as a Postdoctoral Researcher with the Institute of Microelectronics, Tsinghua University, Beijing. From 2013 to 2016, he was a Research Fellow at VIRTUS/EEE, Nanyang Technological University, Singapore. He has been an Assistant Professor with the State Key Laboratory of Analog and Mixed-Signal VLSI (AMSV), University of Macau, Macau, since March 2016. His research interest includes integrated circuit designs involving analog/mixed-signal/RF/mm-wave/sub-THz/wireline. He was a Conference Local Organization Committee Member of A-SSCC, in 2019. He was a member of the IEEE Circuits and Systems Society, Circuits and Systems for Communications (CASCOM) Technical Committee, from 2020 to 2022. He was a Technical Program Committee (TPC) Member of A-SSCC, in 2021; APCCAS, from 2019 to 2021; ICTA, from 2020 to 2021; NorCAS, from 2020 to 2021; ICECS, in 2021; and ICSICT, in 2020. He was a Review Committee Member of ISCAS, from 2021 to 2022. He was a recipient of the second prize in ''Haixi'' (three places across the Straits) Postgraduate Integrated Circuit Design Competition in 2009. He was a co-recipient of the Best Paper Award at the IEEE Asia Pacific Conference on Circuits and Systems (APCCAS), in 2019; the Best Student Paper Award (Third Place) at the IEEE Radio Frequency Integrated Circuits (RFIC) Symposium, in 2021; and the Macao Science and Technology Invention Award (First Prize), in 2020. His team reported 3-chip inventions at the IEEE International Solid-State Circuits Conference—ISSCC (Chip Olympics): mm-wave PLL (2019) and VCO (2019), and radio frequency VCO (2021). From 2019 to 2021, he serves as the Vice-Chair for the IEEE Macau CAS Chapter, where he served as the Chair, from 2021 to 2023; and the Tutorial Chair for ICCS, in 2020. He was the TPC Co-Chair of ICCS, in 2021. He has been serving as an Associate Editor for IEEE Transactions on Very Large Scale Integration (VLSI) Systems, since 2019, and *Electronics Letters* (IET), since 2020. He has been serving as an Editor for *International Journal of Circuit Theory and Applications* (IJCTA), since 2020. He was a Guest Editor of IEEE Transactions on Circuits and Systems—II: Express Briefs, in 2021, and an Associate Editor of IEEE Access, from 2019 to 2021.

PUI-IN MAK (Fellow, IEEE) received the Ph.D. degree from the University of Macau (UM), Macau, in 2006.

He is currently a Professor with the UM Faculty of Science and Technology–ECE, the Interim Director of the UM State Key Laboratory of Analog and Mixed-Signal VLSI, and the Deputy Director (Research) of the UM Institute of Microelectronics. His research interests include analog and radio-frequency (RF) circuits and systems for wireless and multidisciplinary innovations.

Prof. Mak is a fellow of the Institution of Engineering and Technology (IET) and the U.K. Royal Society of Chemistry (RSC). He was a TPC Member of A-SSCC, from 2013 to 2016; ESSCIRC, from 2016 to 2017; and ISSCC, from 2017 to 2019. He (co)-received the 2021 RFIC Best Student Paper Award, the 2005 DAC/ISSCC Student Paper Award, the 2010 CASS Outstanding Young Author Award, the 2011 National Scientific and Technological Progress Award, the Best Associate Editor of the IEEE TRANSACTIONS ON CIRCUITS AND SYSTEMS—II: EXPRESS BRIEFS, from 2012 to 2013, the 2015 A-SSCC Distinguished Design Award, and the 2016 ISSCC Silkroad Award. In 2005, he was decorated with the Honorary Title of Value by the Macau Government. He was the TPC Vice Co-Chair of ASP-DAC, in 2016. He was the Chairperson of the Distinguished Lecturer Program, IEEE Circuits and Systems Society, from 2018 to 2019. He has been inducted as an Overseas Expert of the Chinese Academy of Sciences, since 2018. His involvements with IEEE are: an Editorial Board Member of IEEE Press, from 2014 to 2016; a member of the Board of Governors of the IEEE Circuits and Systems Society, from 2009 to 2011; a Senior Editor of the IEEE JOURNAL ON EMERGING AND SELECTED TOPICS IN CIRCUITS AND SYSTEMS, from 2014 to 2015; an Associate Editor of the IEEE JOURNAL OF SOLID-STATE CIRCUITS, in 2018, the IEEE SOLID-STATE CIRCUITS LETTERS, in 2017, the IEEE TRANSACTIONS ON CIRCUITS AND SYSTEMS—I: REGULAR PAPERS, from 2010 to 2011 and from 2014 to 2015, and the IEEE TRANSACTIONS ON CIRCUITS AND SYSTEMS—II: EXPRESS BRIEFS, from 2010 to 2013. He was a Distinguished Lecturer of the IEEE Circuits and Systems Society, from 2014 to 2015, and the IEEE Solid State Circuits Society, from 2017 to 2018.

RUI P. MARTINS (Fellow, IEEE) was born in April 1957. He received the bachelor's, master's, and Ph.D. degrees in electrical engineering and computers from the Department of Electrical and Computer Engineering (DECE), Instituto Superior Técnico (IST), University of Lisbon, Portugal, in 1980, 1985, and 1992, respectively. He has been with the DECE/IST, University of Lisbon, since October 1980. Since October 1992, he has been on leave from the University of Lisbon and with the DECE, Faculty of Science and Technology (FST), University of Macau (UM), Macau, where he has been the Chair Professor, since August 2013. At FST, he was the Dean, from 1994 to 1997, and has been the UM's Vice-Rector, since September 1997. From September 2008 to August 2018, he was the Vice-Rector (Research) and from September 2018 to August 2023, he was the Vice-Rector (Global Affairs). He received the Habilitation for Full Professor of electrical engineering and computers with the DECE, IST, University of Lisbon, in 2001. In 2003, he created the Analog and Mixed Signal VLSI Research Laboratory, UM, elevated in January 2011 to the State Key Laboratory (SKLAB), China (the 1st in Engineering in Macau), being its Founding Director. He was the Founding Chair of UMTEC (UM company), from January 2009 to March 2019, supporting the incubation and creation of Digifluidic, in 2018, the first UM Spin-Off, whose CEO is a SKLAB Ph.D. graduate. He was also the Co-Founder of Chipidea Microelectronics (Macau) (later Synopsys-Macau, and now Akrostar, where the CEO is one of his Ph.D. graduates), from 2001 to 2002. Within the scope of his teaching and research activities, he has taught 21 bachelor's and master's courses. In UM, he has supervised (or co-supervised) 47 theses and 26 Ph.D. and 21 master's students. He has authored or coauthored nine books and 12 book chapters; 49 patents (39 USA, three Taiwan, and seven China); 675 papers (289 articles in scientific journals and 386 papers in conference proceedings); and other 70 academic works, in a total of 815 publications. He has been a member of the Advisory Board of the *Journal of Semiconductors* of the Chinese Institute of Electronics (CIE), Institute of Semiconductors, Chinese Academy of Sciences, since January 2021, and a fellow of the Asia-Pacific Artificial Intelligent Association, since October 2021. He was also a member of the IEEE CASS Fellow Evaluation Committee, in 2013 and 2014, where he was the Chair, in 2018, and the Vice-Chair, in 2019, 2021, and 2022. He was the Founding Chair of IEEE Macau Section, from 2003 to 2005, the IEEE Macau Joint-Chapter on Circuits and Systems (CAS)/Communications (COM), from 2005 to 2008, and the 2009 World Chapter of the Year of IEEE CAS Society (CASS); the General Chair of the IEEE Asia Pacific Conference on CAS (APCCAS 2008); the Vice-President (VP) Region 10 (Asia, Australia, and Pacific), from 2009 to 2011; and the VP-World Regional Activities and Membership of IEEE CASS, from 2012 to 2013. He was an Associate-Editor of the IEEE TRANSACTIONS ON CIRCUITS AND SYSTEMS—II: EXPRESS BRIEFS, from 2010 to 2013, and nominated as the Best Associate Editor, from 2012 to 2013. He was the IEEE Nominating Committee of Division I Director (CASS/EDS/SSCS), in 2014, and the IEEE CASS Nominations Committee, from 2016 to 2017. In addition, he was the General Chair of the ACM/IEEE Asia South Pacific Design Automation Conference (ASP-DAC 2016), receiving the IEEE Council on Electronic Design Automation (CEDA) Outstanding Service Award, in 2016, and also the General Chair of the IEEE Asian Solid-State Circuits Conference (A-SSCC 2019). From 2005 to 2014, he was the Vice-President of the Association of Portuguese Speaking Universities (AULP), where he was the President, from 2014 to 2017, and the Vice-President, from 2021 to 2024; and has received three Macau Government Decorations— the Medal of Professional Merit (Portuguese-1999); the Honorary Title of Value (Chinese-2001), and the Medal of Merit in Education (Chinese-2021). In July 2010, he was elected, unanimously, as a Corresponding Member of the Lisbon Academy of Sciences, being the only Portuguese Academician working and living in Asia.